

CLOUDS, HAZES, AND METHANE IN THE ATMOSPHERES OF URANUS
AND NEPTUNE: AN ANALYSIS OF SPATIALLY RESOLVED, NEAR
INFRARED SPECTRA

A Dissertation

Presented to the Faculty of the Graduate School
of Cornell University

In Partial Fulfillment of the Requirements for the Degree of
Doctor of Philosophy

by

Michael Thomas Roman

August 2015

© 2015 MICHAEL THOMAS ROMAN

CLOUDS, HAZE, AND METHANE IN
THE ATMOSPHERES OF URANUS AND NEPTUNE:
AN ANALYSIS OF SPATIALLY RESOLVED, NEAR INFRARED SPECTRA

Michael Thomas Roman, Ph. D.

Cornell University 2015

Spatially resolved, near-infrared spectral observations of Uranus and Neptune are presented and analyzed in this study of the ice giant atmospheres. Using radiative transfer analysis and a sophisticated constrained retrieval algorithm, the distribution of aerosols and methane gas were retrieved from H and K-band near-infrared spectra. These observations cover a range of latitudes and times between 2001 and 2007, permitting significant spatial and temporal variance in the retrieved quantities. Two layers of aerosols are needed to match the near-IR observations of both Uranus and Neptune. The upper layer peaks near the tropopause on Uranus and in the lower stratosphere on Neptune. The layer is considerably thicker and more variable on Neptune, producing the prominent clouds visible in near-IR images of Neptune. The lower cloud peaked at ~ 2.1 and ~ 2.3 bars for Uranus and Neptune, respectively, with variations in latitude that are interpreted in context of notional circulation models. Temporal changes suggest potential seasonal effects in the case of Uranus and intra-seasonal variation on Neptune. Retrievals of the methane mole fraction are consistent with polar depletion on both planets, although Neptune has more methane at the tropopause with which to produce condensate. Finally, high clouds on each planet are considered in terms of parcel theory with the goal of understanding formation mechanisms. The low scattering optical depths of discrete high clouds are consistent with formation associated with vortices and shallow lift rather than deep convection.

BIOGRAPHICAL SKETCH

Michael Roman transferred into Cornell University in 2004 as a junior in the field of Atmospheric Sciences, after having studied at a small community college. As an undergraduate, he became involved in research as a student research assistant, organizing and processing image data from the Galileo mission. The project combined two of his of long-lived interest—astronomy and meteorology—and encouraged him to pursue further research experience. After receiving his Bachelor of Science degree from the College of Agriculture and Life Sciences in 2006, he continued working as a research assistant under the supervision of Professor Peter Gierasch and Dr. Don Banfield. After two years of work, he enrolled as a graduate student in the field of Atmospheric Sciences at Cornell University, with his previous supervisors now serving as his academic advisors.

I wish to dedicate this work to those who have allowed me the opportunity to explore my interest and passions while maintaining gainful employment a surprising majority of the time. It has been a privilege working with such outstanding, well-rounded individuals, whose teachings ranged from lessons in radiative transfer and image processing to lock picking and driving stick. I also wish to dedicate this to all past and future friends of the Fuertes Observatory; from observing through the 12" refractor to rummaging through the basement treasures, my many hours in the observatory have left an indelible mark on my life. Thanks for helping to keep the place alive and well.

ACKNOWLEDGMENTS

This dissertation would not have been possible without the generous and patient support of my advisors, Prof. Peter Gierasch and Dr. Don Banfield, as well as my additional committee members Profs. Joe Veverka and Peter Hess. This was no easy task on their part. I suspect Peter Gierasch, the paragon of patience, had on many occasions cycled to campus with hopes of discussing interesting dynamics, only to find me endlessly fussing with tedious retrievals. Similarly, I fear that Don Banfield may have endured a few extra cross-country flights only to share in this disappointment. In fact, by the time I finally did get around to discussing dynamics, Joe Veverka actually had to come out of retirement to hear about it. That said I might have never completed this analysis without the brilliance of Barney Conrath, whose theoretical and practical understanding of retrieval algorithms provided the framework I myself could not devise. Daphne Stam also deserves thanks for adapting hydrogen absorption coefficients from Borysow, saving me the frustration. Funding, in part, was made possible by a NASA Planetary Astronomy grant NNG05GH57G (observations) and a NASA Outer Planet Research grant NNX09AU25G (analysis). Last but not least, I wish to acknowledge the observers, namely Don Banfield, Phil Nicholson, Daphne Stam, and Barney Conrath, among others, whose data extended my stay in lovely Ithaca by seven years.

TABLE OF CONTENTS

BIOGRAPHICAL SKETCH	iv
DEDICATION	v
ACKNOWLEDGMENTS	vi
TABLE OF CONTENTS	vii
LIST OF FIGURES	viii
LIST OF TABLES	ix
PREFACE	x

CHAPTER 1. URANUS

1. Introduction	1
2. Data	3
2.1 Deconvolution	6
3. Analysis	8
3.1 Spectra	7
3.2 Atmospheric Model	12
3.2.1. Methane Profile	12
3.2.2 Aerosol Scattering and Reflectance.....	14
3.3 Retrieval Algorithm.....	18
3.3.1 Retrieval Uncertainties	19
4. Results	21
4.1 Mean Results	21
4.2 Latitudinal Variation	26
4.3 Lone Cloud Feature	31
5. Discussion	34
5.1 Cloud Structure and Seasonal Changes	34
5.2 Discrete Cloud Formation	39
5. Concluding Summary	45

CHAPTER 2. NEPTUNE

1. Introduction	48
2. Data	50
3. Analysis	54
3.1 Spectral transmission and parameter sensitivities	54
3.2 Atmospheric Model	55
3.2.1. Modeled Methane Profile	57
3.2.2 Aerosol Scattering and Reflectance.....	58
3.3 Retrieval Algorithm.....	59
3.3.1 Retrieval Uncertainties	60
4. Results	62
4.1 Retrieved scattering optical depth	62
4.2 Retrieved methane mole fraction.....	71
5. Discussion	74
5. Concluding Summary	80

REFERENCES 82

LIST OF FIGURES

CHAPTER 1

Figure 1. Sub-solar latitude as a function of time for Uranus and Neptune	3
Figure 2. Atmospheric Transmissions for Uranus.....	9
Figure 3. Methane models for Uranus	13
Figure 4. Comparison of single scattering to multiple scattering.....	17
Figure 5. Ensemble plot of paramter uncertainties, Uranus	20
Figure 6. Annual mean retrieved scattering optical depths, Uranus.....	24
Figure 7. Annual mean retrieved methane mole fractions, Uranus	25
Figure 8. Goodness of fit comparisons for deep methane models, Uranus	26
Figure 9. Retrieved cross sections 2001 and 2007, Uranus.....	28
Figure 10. Retrieved cross sections 2001-2007, Uranus	29
Figure 11. Vertically integrated scattering optical depths vs latitude, Uranus.....	30
Figure 12. Retrieved 100 mb methane mole fraction versus latitude, Uranus	31
Figure 13. H and K-band images and spectra showing discrete feature	32
Figure 14. Observed spectra for discrete feature and adjacent locations	33
Figure 15. Retrieved aerosol profile for discrete feature.....	33
Figure 16. Retrieved cross section for observation featuring discrete feature	34
Figure 17. Thermodynamic diagram for discrete feature, Uranus	44

CHAPTER 2

Figure 1. H and K-band images of Neptune.....	52
Figure 2. H and K-spectral images of Neptune	53
Figure 3. Atmospheric transmissions for Neptune	56
Figure 4. Ensemble plot of paramter uncertainties, Neptune	61
Figure 5. Retrieved cloud heights, Neptune	63
Figure 6. Retrieved profile of scattering optical depths, Neptune.....	64
Figure 7. Retrieved profile of scattering optical depths at 40°S and 1°N, Neptune	65
Figure 8. Representative cross section and methane methane abundance, Neptune	66
Figure 9. Retrieved cross sections, Neptune	67-69
Figure 10. Vertically integrated scattering optical depths vs latitude, Neptune.....	70
Figure 11. Retrieved methane profiles, Neptune.....	72
Figure 12. Retrieved 60 mbar methane mole fraction vs latitude, Neptune	73
Figure 13. Retrieved m-amagats of methane vs latitude, Neptune.....	74
Figure 14. High albedo vs low albedo scattering optical depths, Neptune	78

LIST OF TABLES

CHAPTER 1

Table 1. Observations of Uranus	4
Table 2. Results for Uranus	22

CHAPTER 2

Table 1. Observations of Neptune	51
--	----

PREFACE

Uranus and Neptune present some intriguing characteristics that we do not yet understand. Compared to the other outer planets, Uranus' extreme axial tilt means its poles are in sunlight or shadow for decades at a time. This would presumably produce some dramatic seasonal effects, but our observations of such are still very limited. Uranus also has a remarkably low internal heat flux, which may affect atmospheric convection and circulation, but we have yet to understand why this is the case and what affects it may have. Though similar in size and mass to Uranus, Neptune presents a different set of puzzling traits. Neptune appears to have the strongest winds in the solar system despite its great distance; from a terrestrial perspective, this is surprising since solar heating ultimately drives terrestrial winds. Intriguingly, observations also show a greater abundance of methane in the lower stratosphere than one would expect possible given the temperature profile. Such observations challenge our understanding of circulation and flow in planetary atmospheres.

Our understanding of the ice giants, Uranus and Neptune, has been hindered in part by their great distances. At 20 and 30 AU from the Sun, Uranus and Neptune are challenging targets. For the first two hundred years since it was first recognized for a planet, even with the world's largest telescopes, Uranus appeared as a slight disk. Neptune, being even farther was worse. The small angular sizes of their disks in the night sky—never greater than $\sim 2 \frac{1}{3}$ arc seconds in the case of Neptune—are easily overwhelmed by the limitations of seeing through Earth's atmosphere. In spite of this, there were still things that could be learned. Photometry showed variations in the

brightness over time (e.g. Lockwood and Jerzykiewicz, 2006). Spectroscopy showed that the upper troposphere of Uranus was relatively cloud free, implying the clouds were deeper than observed on Jupiter and Saturn. The spectrum of Uranus also provided the first identification of molecular hydrogen in any astronomical source (Herzberg, 1952). Stratospheric and high altitude observations in the 1970s showed that they were both very cold—less than 60 K (e.g. Morrison and Cruikshank, 1972). The two planets were seen as nearly identical in composition and proportions, but not much could be said about their appearance. We could not see the atmospheric circulations and clouds as they were seen on Jupiter and Saturn. Voyager II's tour of the outer solar system was intended to change this.

Voyager II arrived at Uranus in 1986. After a two hundred year wait, astronomers were afforded their first close up view of what had been little more than a featureless disk. Images of the southern summer hemisphere, illuminated nearing solstice, showed only a few discrete cloud features on an otherwise indistinct planet. Recent reanalysis of the Voyager II data, reprocessed and averaged to enhance the contrast, has revealed greater complexity of spots and zonal banding than previously realized (Karkoschka, 2015), but the planet was clearly less meteorologically active than its more distant neighbor. Neptune, as encountered in 1989, was marked with several distinct features, including a large, dark vortex, which swirled as rapidly changing, white clouds seemingly skirted far above.

Voyager II was simply a flyby of these planets, and so it only provided a glimpse of a long seasonal cycle. To learn about potential seasonal changes, continued observations were needed. By the 1990s, the Hubble Space Telescope

(HST) came online allowing for more spatially resolved observations. Then by 2000, adaptive optics technology matured, permitting views from the Earth's surface with less atmospheric distortion than ever possible before. With spatially resolved images and spectra more readily available, observations began to show changes in the spatial distribution of cloud, hazes, and gases. Such observations can be used to infer details about the environments in which clouds form and the physical processes at work. That is the motivation behind this present study.

Spatially resolved, near-infrared spectral observations of Uranus and Neptune, dating from 2001 to 2007, were acquired for this study of the ice giant atmospheres. Data were collected by a number of observers including Don Banfield, Phil Nicholson, Daphne Stam, and Barney Conrath among others, and reduced and calibrated by the author. Applying radiative transfer analysis and a sophisticated constrained retrieval algorithm to H and K-band near-infrared spectra, the distribution of aerosols and methane gas were retrieved.

Aerosol scattering optical depths and methane mole fractions on both Uranus and Neptune showed temporal and spatial variability. Two distinct layers of aerosols were found in all cases.

On Uranus, observations were consistent with an optically very thin haze near the tropopause and a deeper, thicker haze or cloud layer at ~ 2.1 bars. The lower layer exhibited changes in reflectance with latitude and time. Scattering optical depths were found to be greatest in the southern hemisphere, centered at $\sim 50^\circ$ S in 2001. From 2001 to 2007, the total scattering optical depth of the deeper layer diminished by a factor of three or more, particularly at southern summer latitudes, resulting in a more

roughly symmetric distribution. This analysis adds to a limited but growing body of observations documenting temporal changes on Uranus.

The changes in reflectance from 2001 to 2007 appeared to be linked to seasonal change as Uranus arrived at equinox, suggesting insolation strongly affects the aerosol distribution. Given potentially long radiative and dynamical time scales, the relatively rapid changes may be attributed to changes in aerosol scattering properties, specifically modest reductions in particle size and scattering phase function; however, the present data cannot distinguish between several potentially changing scattering properties and potential changes in aerosol abundance. Future research utilizing center-to-limb analysis over a wide range of wavelengths will likely be needed to determine the which factors contribute to the observed temporal changes.

The overall distributions of aerosols were consistent with—but not strongly discriminating of—speculative circulation models that include at least two layers of circulation cells at different latitudes and pressures. Such models may explain the change in cloud heights and reflectance seen at $\sim 45^\circ\text{S}$.

Best fits to the data were achieved with a methane distribution that decreased towards the poles, consistent with the findings of recent studies (Karkoschka and Tomasko, 2009) and circulation models with downwelling at the poles. The methane mole fraction at the tropopause was retrieved with an average value of $(2.7 \pm 1.6) \times 10^{-5}$, significantly below saturation and consistent with previous findings (Orton et al., 2014). No significant variations in latitude were detected, but a factor of four increase was noted from 2001 to 2005—larger than can accounted for by estimated

uncertainties. Potential temporal changes in the 100-mbar methane mole fractions have not been previously investigated and thus require additional study.

Finally, a discrete cloud feature of unusual height was analyzed. Despite the relative brightness, the cloud's observed reflectance, retrieved scattering optical depth, and inferred aerosol mass are very low. All together, the results favor the interpretation of this and similar cloud features as bright companion clouds associated with dark or unseen vortices.

In the case of Neptune, the upper layer shows significant temporal and spatial variability at a height above the tropopause. The scattering optical depths of this layer were greatest at southern mid-latitudes, particularly in 2001 and 2002, though from 2003 to 2007, these latitudes diminished in reflectance. Similar variations have been noted by other researchers (e.g. Karkoschka, 2011), but the cause remains unknown. The retrieved heights and optical thicknesses are consistent with lift occurring in the lower stratosphere and thus consistent with models of slow upwelling and resultant anticyclonic vortex companion clouds as opposed to violent, penetrative convection.

The deeper cloud layer was relatively more uniform than the upper layer, but still displayed up to a factor of three variations in scattering optical depths. With a peak at ~ 2.3 bars, the greatest optical depths were also found at southern mid-latitudes in 2001 and 2002. Together, both layers suggest a circulation with upwelling at mid-latitudes with a vertical extent of several pressure scale heights, consistent with conclusions drawn from thermal, near-IR, and microwave data (Conrath et al., 1990; Conrath et al., 1998; dePater et al., 2014).

The retrieved methane profiles show marginal temporal and spatial variability. All retrievals require a methane mole fraction in the lower stratosphere that exceeds the expected tropopause cold trap value. Higher methane mole fractions appear to be roughly correlated with latitudes of enhanced aerosols scattering optical depth and theorized upwelling, though only marginally so given the retrieval uncertainties and apparent variability. The 60-mbar mole fractions are consistently less than other published values by a factor of 3 to 10. This may reflect differences in the observations as well as the modeling. Future analysis using different data and techniques may be necessary to better constrain the true value and explain the apparent discrepancy.

Finally, the temporal variation in high cloud cover on Neptune may be related to changes in the methane mole fraction. Such variations may ultimately result from changes in the intensity of upwelling. Periods of greater upwelling result in greater methane saturation and more cloud cover at mid-latitudes. The fact that Neptune has appeared more active than Uranus in past decades may be related to the difference in internal heat fluxes between the two planets; internal heating may drive circulation cells over greater vertical lengths on Neptune, pumping more methane higher into the atmosphere, ultimately leading to the prominent clouds and hazes that differentiate Neptune in appearance from Uranus.

Questions concerning seasonal changes and atmospheric dynamics in the ice giants clearly remain. Given the great distances and long seasons, increased understanding of the structure and dynamics of these worlds will only come through continued remote measurements of their observable features for decades to come.

Leaps in our knowledge will ultimately require observations by future spacecraft missions, as we have seen for the other planets in our solar system.

CHAPTER 1

AEROSOLS AND METHANE FROM NEAR-IR SPECTRA: URANUS

1. Introduction

For more than 200 years following Herschel's discovery, the planet Uranus appeared as little more than a small, featureless disc. With its great distance and slight angular size, Uranus had challenged observers and provided few visual details compared to Jupiter and Saturn. Spectroscopic studies suggested a relatively clear upper troposphere with clouds forming deeper than observed on the gas giant planets. This impression of a nearly featureless world, lacking the visual splendor of Jupiter and Saturn, was only strengthened when Voyager II encountered Uranus in 1986; images of the southern summer hemisphere, illuminated nearing solstice, showed only a few discrete cloud features on an otherwise indistinct planet.

In recent years, this picture of a vague, featureless planet has begun to change. Increasingly sophisticated technology has improved our ability to observe the atmosphere during the last two decades. With the emergence of adaptive optics and better imaging techniques in the late 1990s, Earth based observers have recorded an increasing number and intensity of discrete cloud features (Karkoschka, 1998, 2001; Sromovsky et al. 2000; Sromovsky and Fry, 2005; Sromovsky et al., 2007; de Pater et al., 2015). Sophisticated image processing techniques have extracted greater details of the latitudinal banding (Fry et al., 2012). Even recent reanalysis of the Voyager II data, reprocessed and averaged to enhance the contrast, has revealed greater complexity of spots and zonal banding than previously realized (Karkoschka, 2015). On top of this, Uranus appears to have become intrinsically more active in recent

years. 2014 Keck observations show clouds of unprecedented brightness and prevalence (see de Pater et al., 2015). The prominent bright features at near-infrared wavelengths are in stark contrast to uniform hazes in Voyager images.

As our visual picture changes, spectroscopic studies continue to reveal additional information on the Uranian atmosphere's vertical structure. Spectrographs fitted with adaptive optics can provide data on the vertical distribution of hazes and gases at different locations on the planet's disc. Cloudy regions can be contrasted with clearer regions to investigate cloud dynamics, and changes with latitude may provide insight into the general circulation. Over time, such observations can help to reveal how seasonal changes influence the haze distributions and cloud activity.

In the present study, near-infrared (NIR) spectral data of Uranus covering a period from 2001 to 2007 are introduced and investigated. Using a constrained inversion algorithm, vertical profiles of clouds and hazes are retrieved over a range of latitudes. Changes in the clouds and hazes are reported, and an unusual isolated cloud feature is analyzed. Section 2 describes the data set, followed by the analysis techniques in section 3, and results in section 4. Section 5 presents a discussion of the results, concluding with a summary in section 6.

2. Data

Observations of Uranus were made annually between 2001 and 2007 at Palomar Observatory, using the 200-inch (5.1m) Hale Telescope and the Palomar High Angular Resolution Observer (PHARO) near-infrared adaptive optics (AO) camera system (Hayward, 2001). The PHARO instrument captured spatially resolved images and spectra in both the H (1.487-1.783 μm) and K (2.028-2.364 μm) bands.

The slit of the spectrograph was aligned roughly along the planet's central meridian, yielding spectra as a function of latitude across the disc. Data were collected by a number of observers including Don Banfield, Phil Nicholson, Daphne Stam, and Barney Conrath among others.

This observing period covers about 1/12 of a Uranus orbit (84 years), and includes the 2004 Uranus equinox, marking the seasonal passage of the sub-solar latitude northward across the equator (see Fig 1). For reference, Voyager 2 had observed the southern hemisphere during the preceding solstice. While the present observations were made over multiple nights each year from 2001 to 2007, many nights failed to yield sufficiently reliable data due to poor AO performance, bad seeing, or sub-optimal photometric conditions; as a result, no data from 2003 and 2006 are included in the analysis (see Table 1). Solar phase angles were less than 1° .

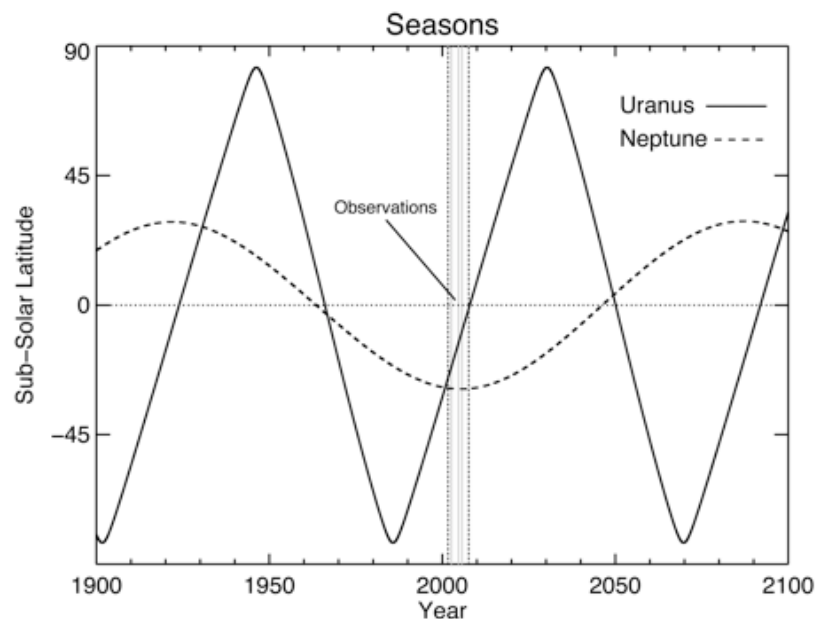


Figure 1. The Sub-solar latitude is plotted as a function of year to illustrate the seasonal coverage of the data set. Observations cover a period of six years from late southern-summer to equinox.

Table 1. Observations Dates, Start Times (UTC)

(year-month-day, hr:mn)

2001-09-03, 08:07
2001-09-04, 08:40
2002-08-24, 09:09
2002-08-24, 09:38
2002-08-25, 09:26
2002-08-26, 09:20
2002-08-26, 09:52
2004-07-25, 10:28
2004-07-25, 10:56
2004-07-28, 11:25
2004-07-28, 11:53
2005-09-16, 07:59
2005-09-16, 08:30
2005-09-16, 08:56
2005-09-16, 09:24
2007-08-15, 11:34
2007-08-15, 12:04
2007-08-17, 09:13
2007-08-17, 09:47
2007-08-17, 10:16

Images of Uranus in the H-band showed a mostly bland disc marked with a few distinguishable features. A bright band, commonly referred to as the south polar collar, was visible over the entire period of observations. An accompanying discrete feature, as noted by others was also observed (Sromovsky et al., 2009). Occasional discrete cloud features were seen at mid-northern latitudes. With the exception of a single feature visible in 2007, none of the aforementioned features were seen in the K-band images. Due to gaseous absorption, K-band images and spectra were extremely dark with very low signal relative to noise; the most obvious feature of these images

and spectra are the Uranian rings, exposed by the long integration times needed to increase the signal to noise ratio. The data were reduced and photometrically calibrated (by the author) using standard techniques for near-infrared spectra and images, including flat fielding, sky-subtraction, and interpolation to remove bad pixels. The faint standard star, FS34 was used for flux calibration, while a number of solar-type stars (SAO 163989, SAO 164580, SAO164338, SAO 146135, SAO 163616) were used as solar proxies, allowing us to express the calibrated spectra into dimensionless units of I/F.

Spectra were calibrated in wavelength by comparison with known spectral lines of planetary nebula NGC 7027 and carefully corrected to remove errors due to imperfect sky subtraction and occasionally detectable tilts of the slit relative to the detector.

At a resolution of 40 mas per pixel, Uranus covered ~ 93 pixels in diameter in the 1024 X 1024 array images, with corrected seeing discs estimated to range between four to seven pixels in diameter near the planet center based on the full-width at half maximum of Uranian satellites. This corresponded to a resolution of roughly 2160 km to 3780 km at the sub-observer point on Uranus, depending on the seeing and AO performance, and was far short of being diffraction limited.

Passing through a 0.5 arc second slit (~ 13 pixel), the observed flux was dispersed by grating prism across the 1024-pixel detector at a resolution 0.285 and 0.332 nm/pixel for H and K, respectively, with resolving powers of roughly $R \sim 1500$. The final calibrated spectra were binned by a factor of 13 to match the spectral resolution set by the spectrographs' projected slit width.

2.1 Deconvolution. Though adaptive optics largely corrects for the atmospheric seeing, residual blurring still alters the spatial distribution of the flux. Light along the edge of the planetary disk blurs with the sky beyond the disk, reducing the observed flux along the edge of the planet. Likewise, neighboring dimmer regions reduce the flux from distinctly brighter regions on the disk. This blurring can be modeled as the convolution of the true image (i.e. the image prior to being distorted by the atmosphere) and the point spread function (PSF) of the Earth's atmosphere (Karkoschka, 2001; Sromovsky and Fry, 2007). The true image could then be largely restored by de-convolving the observed image with the correct atmospheric PSF, with the cost of amplifying the noise (e.g. see Sromovsky and Fry, 2007). Some additional smoothing is required to correct for the increased noise, typically in the form of Gaussian convolution. The correct PSF is a function of time, position, and wavelength, but it may be estimated from the image data itself if one assumes the brightness distribution of the true disk.

Deconvolving the spectra is not as simple, since the spectral observations are in one spatial dimension while the blurring occurs in two spatial dimensions; the flux lost beyond the edges of the slit cannot be recovered in the spectral images, and the 1-dimensional PSF required for a 1-d deconvolution would need to be artificially adjusted to compensate for this loss. Furthermore, the spectral deconvolution significantly amplifies the noise, and in darker regions of the spectra this increased noise can easily dominate over the signal. For these reasons, deconvolving the spectra introduces the risk of corrupting the true data.

We chose to take a conservative approach: all of the data was analyzed without applying deconvolutions; then to assess the potential affect on the results, representative cases from 2001 and 2007, representing the end points of the time span, were deconvolved and analyzed. For these two cases, deconvolutions were performed only on the image observations to avoid uncertain manipulations of the spectra, and the modified image flux was then used to calibrate the spectra. The atmospheric PSF was estimated by convolving a sharp synthetic featureless disk, representing the true disk image, with an adjustable PSF (with a functional form as applied by Stromovsky and Fry, 2007); PSF parameters were adjusted until the synthetic disk matched the observed disk; this PSF was assumed to match the atmospheric PSF and hence used to deconvolve the observations. A Gaussian with a full-width at half-maximum of 4 was employed in the deconvolutions to keep the noise from increasing by more than 10%. The resulting H spectra are overall brighter—by up to 30% brighter for locations corresponding to near edges and discrete bright features. Results derived from these deconvolved cases are included with the other results in Section 4.

3. Analysis

3.1 Spectra.

Aerosol scattering and molecular absorption of sunlight shape the spectra of Uranus in the H and K bands. At these near-infrared wavelengths, Rayleigh and Raman scattering are insignificant, and molecular absorption would cause the atmosphere to appear dark in the absence of aerosols. The observed spectra can be

nearly completely explained by the light scattered by aerosols and attenuated by methane and collisional-induced absorption (CIA) by hydrogen.

The wavelength dependence of the molecular absorption can be seen in a plot of transmission depths computed from gaseous absorption coefficients. Figure 2 shows the atmospheric pressure heights corresponding to a single optical depth of attenuation along the two-way path for reflected sunlight at normal incidence. The calculations assume a stratospheric methane mole fraction of 2.5×10^{-5} and a deep methane abundance of 3.2% for pressure greater than 2 bars, consistent with modeling results. Methane is the primary absorber in the H-passband, but the wavelength dependence of the absorption results in a wide range of vertical sensitivities. In the center of the H-band, the wavelength-dependent methane absorption is relatively weak, and incident light can penetrate and return from several bars of pressure before it is considerably attenuated. Towards the edges of the band, the absorption is greater and radiation is equally attenuated over a much shorter path length. Through much of the K-band, absorption due to the collisional induced dipole of molecular hydrogen (hydrogen-hydrogen and helium-hydrogen collisions) dominates over the methane absorption. In the hydrogen-rich atmosphere of Uranus, this serves as a significant source of opacity. Optical depths of unity are reached at pressures less than a few hundred millibars, making the K-band sensitive to the tropopause and lower stratospheric heights. At the longest K-band wavelengths, methane once again becomes a significant source of opacity, comparable in contribution to hydrogen CIA.

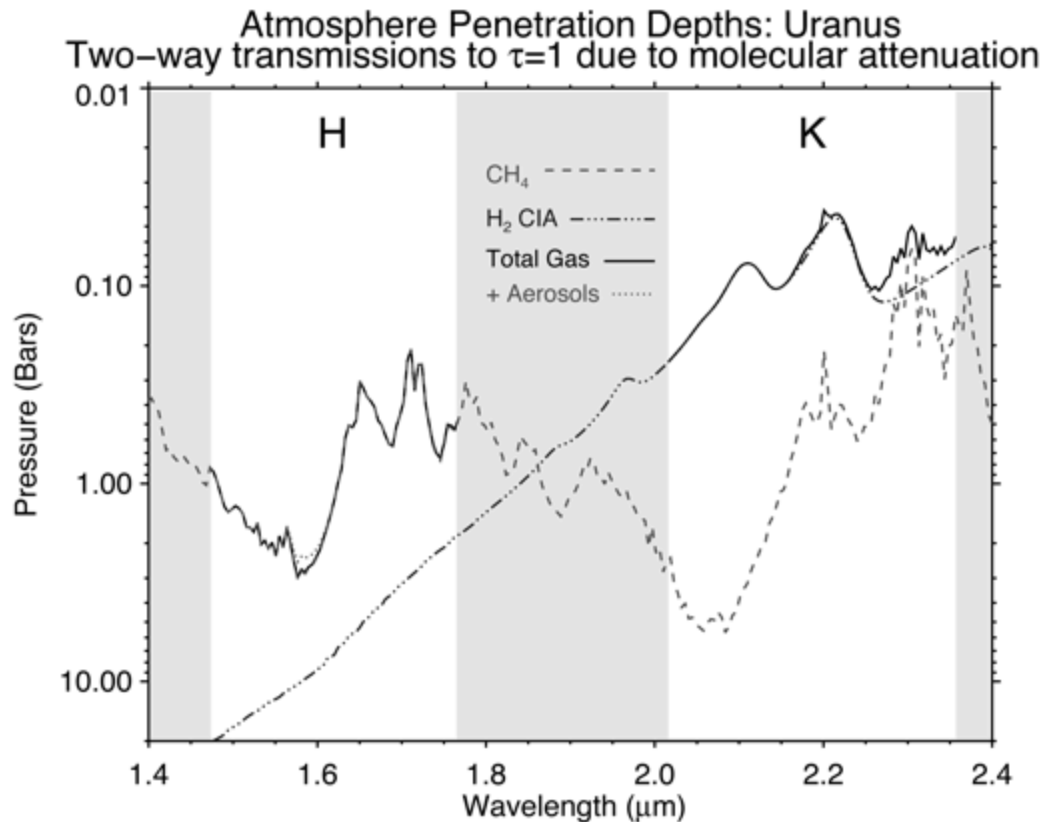


Figure 2. Atmospheric pressure heights corresponding to a single optical depth of attenuation along the two-way path for reflected sunlight at normal incidence. Different components to the attenuation are plotted separately. Weak methane absorption dominates in the H-band; collisional induced absorption by hydrogen dominates the K-band. Wavelengths beyond the filter ranges are shaded in gray. Aerosols only become significant in the deepest sensing regions of the H-band.

Assuming that the atmospheric mixing ratio of hydrogen is well constrained, then the atmospheric opacity in the K band (where hydrogen absorption dominates) may be reliably computed. Given this, the observed reflectance at these wavelengths can be used to determine the necessary reflectance (i.e. effective optical thickness) produced by aerosols at the related wavelengths corresponding to the same pressure levels. With the assumed range of opacities and resulting transmission depths, the vertical distribution of aerosols in the atmosphere can be reliably inferred between 60

mbar and 300 mbar. Below these heights, the inferred aerosol abundance depends on the methane abundance.

Unlike hydrogen, methane condenses in the cold tropospheric temperatures of Uranus' atmosphere; therefore, the mixing ratio of methane potentially varies with height and location. The observed reflectance at wavelengths dominated by methane opacity cannot be used to uniquely constrain the aerosol distribution; however, if the aerosol reflectance is independently determined by using the known hydrogen opacities, then some constraints can be placed on the methane abundance. The total methane abundance above a defined aerosol layer may then be inferred, and the vertical distribution of methane can be resolved if the aerosol abundance at each height is known. The latter requires observations at two points of the spectrum—one at wavelengths dominated by methane absorption and the other at wavelengths dominated by hydrogen CIA— but with similar transmission functions so that they are sensing reflecting aerosols at the same heights. If this condition is not met, the methane distribution cannot be uniquely determined.

Examining Fig. 2, we can see that methane clearly dominates in the H-band and hydrogen CIA dominates in the K-band, but the amount of overlap in transmission functions depends on the methane abundance. For the average methane abundances retrieved from the present data, the methane absorption features at roughly 1.7 and 2.3 microns are strong enough to extend high into the hydrogen absorption dominated heights where the aerosol reflectance can be constrained; thus, the methane mixing ratio can be uniquely determined at roughly 200 mbar and 70-100 mbar if the aerosol reflectance is assumed to be roughly wavelength independent. Additionally, regardless

of the precise distribution, the total observed reflectance could be used to constrain the cumulative methane abundance above the deepest observed cloud layer.

Deeper in the atmosphere, the spectra provide less constraint. The hydrogen CIA becomes optically thick at much higher heights and cannot be used to uniquely constrain the aerosols; consequently, the aerosol and methane distribution deeper than a few hundred millibars become ambiguous. With these limitations, a potential aerosol profile may be retrieved if an assumed methane profile is fixed. This was the course taken for this study, as discussed in details of the model below.

3.2 Atmospheric Model.

A 1-D atmospheric model was used to produce synthetic spectra. The model consisted of 70 vertically stacked layers ranging from 20 bars to 1 mbar. Each layer was effectively defined by its methane and aerosol abundance, forming vertical profiles of each variable. Opacities for methane were computed using absorption coefficients as prescribed by Sromovsky et al. (2012). Hydrogen CIA opacities were computed using coefficients of Borysow (1996), adapted for arbitrary para-hydrogen fractions; the fraction was initially a free parameter, but subsequent testing demonstrated that the precise values could not be constrained by this data set, and it was thus set to the local thermodynamic equilibrium fraction. Since the gaseous absorption is a function of pressure and temperature, a standard temperature-pressure profile from Voyager radio occultation data (Lindal et al., 1987, model F) was used; other published profiles were tested (e.g. Lindal et al., 1987 model D; Sromovsky et al., 2011), but the results were not significantly sensitive to differences in these temperature profiles.

3.2.1. Methane profile.

Given the limitations of the data, additional constraints must be placed on the vertical distribution of methane. The data can potentially constrain the methane mole fraction around the tropopause if the abundance is sufficiently high, or else provide the accumulated column abundance above several hundred millibars if sufficient aerosol is present. Below these heights, the abundance must be assumed. Published values for the deep methane mole fraction include 2.3% from Lindal et al. (1987), 3.2% from Karkoschka and Tomasko (2011), and 4% from Sromovsky et al. (2011) and Sromovsky et al. (2014). The latter three studies also suggested equator-to-pole variation, with methane depletion at the pole. For the present study, calculations were done for four different assumptions in order to evaluate the effect on the results. The first assumed a constant mixing ratio of 4% at pressures greater than 1.4 bar for all latitudes (Sromovsky et al. 2011); the second case was latitude dependent, with the CH₄ mole fraction dropping smoothly from 4% at the equator to 2% at the poles, based on a smooth version of latitude dependence given in Fig. 12 of Sromovsky et al (2014); the third case followed Karkoschka and Tomasko (2011) with a fixed deep abundance of 3.2%, but with the height of this layer pushed deeper towards the poles (from their Figure 10). The fourth case was based on Sromovsky et al (2014) and assumed a 4% deep abundance with a different latitude dependent height (see their figure 17). In all assumptions, a north-south symmetry was assumed.

To complete the methane vertical profile, the deep and tropopause values were smoothly connected with two additional constraints. Firstly, the mole fraction was constrained to remain below saturation, as determined by the saturation vapor pressure

and temperature profile (Lindal et al, 1987). Secondly, given the deep source of the methane, the mole fraction could not increase with height. This results in a family of profiles like those illustrated in figure 3.

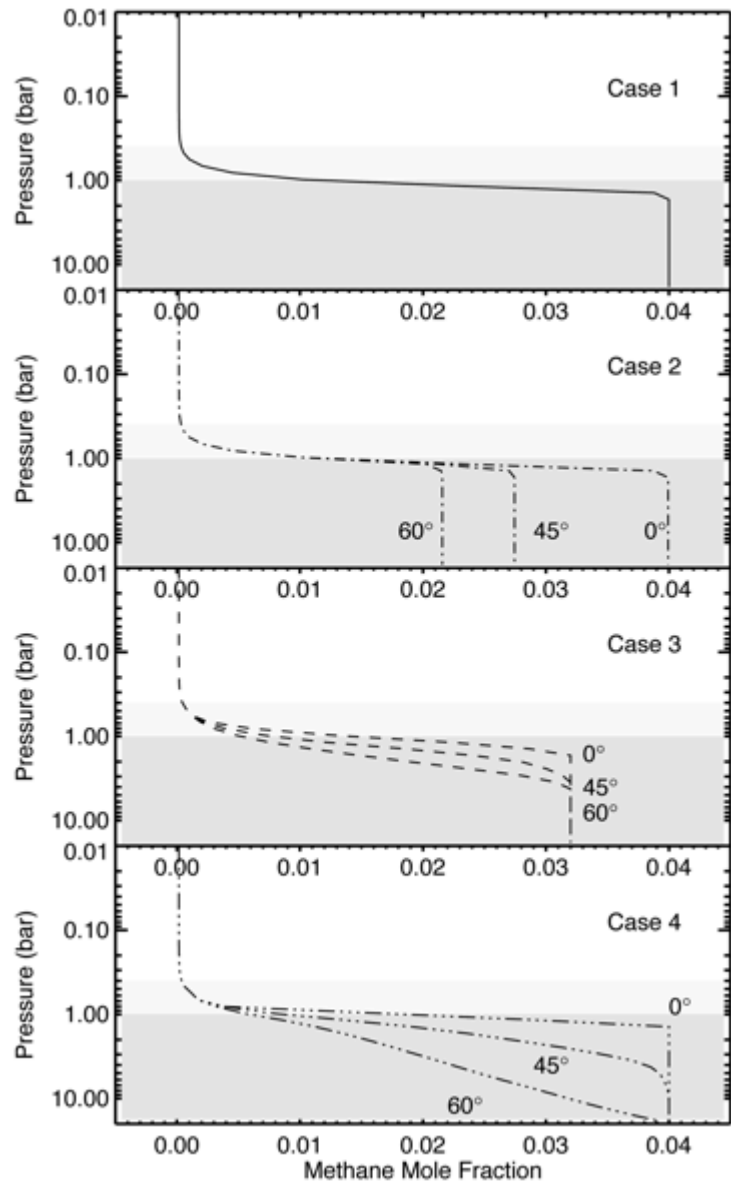


Figure 3. Four different models for the methane distribution to be evaluated by the retrievals. Cases 2-4 assume latitude dependence, while Case 1 does not. Pressures not shaded are free to vary; pressures shaded in dark gray are fixed; lightly shaded regions transition between the fixed and free. More details are provided in the text.

Note that no effort was made to ensure that methane profiles were self-consistent with retrieved cloud condensation heights or the inferred cloud height in the Voyager radio occultation results. Indeed, given the Lindal et al. (1987) temperature profile, none of these methane profiles reach saturation on average. This apparent incompatibility may be resolved by reducing the temperature profile, as shown possible by the Sromovsky et al. (2011) reanalysis of the Voyager refractivity data, or by simply regarding the profiles as spatial averages of saturated and unsaturated regions, as Lindal et al (1987) suggested.

3.2.2. Aerosols Scattering and Reflectance

Aerosols distributions were modeled following methods of Banfield et al. (1996, 1998) and Stam et al (2001). Each layer of the atmosphere had an optical thickness of gas and aerosols; the aerosol component scattered light and resulted in the observed reflectance.

In a single-scattering regime, the contribution to the observed reflectance from each layer is dependent on the number of aerosols in the layer, n , the effective cross sectional area of each particle, σ , the single scattering albedo of the aerosols, ϖ_0 , and the normalized scattering phase function evaluated at the angle between light incidence and emission, $PF(\alpha)$. The product of these terms is here referred to as the scattering optical depth, τ_s :

$$\tau_s(z, \lambda) = n(z) \sigma(z, \lambda) \varpi_0(z, \lambda) PF(\alpha, z)$$

Where z and λ designate that parameters are a function of height and wavelength. The total reflectance due to single scattering can be found by vertically integrating over all layers down to sufficiently great atmospheric optical depths:

$$I(\lambda) = \frac{F(\lambda)}{4} \int_0^\infty n(z) \sigma(z, \lambda) \varpi_0(z, \lambda) PF(\alpha, z) e^{-\tau(z, \lambda)\mu_0} e^{-\tau(z, \lambda)\mu} \frac{dz}{\mu}$$

Where $I(\lambda)$ and $\pi F(\lambda)$ are the observed and incident solar flux at wavelength λ , $\tau(z, \lambda)$ is the total atmospheric optical depth from the top of the atmosphere down to height z , and μ_0 and μ are the cosines of the incidence and emission angles, respectively. Assuming hydrostatic balance, the height could be expressed in pressure coordinates. Given a range of atmospheric weighting functions, one can potentially invert the observations of $I/F(\lambda, \mu, \mu_0)$, to retrieve the scattering optical depth, τ_s , as a function of pressure for each wavelength.

The wavelength dependence of the scattering optical depth was modeled by letting the effective scattering cross section, σ , vary. Theoretical wavelength dependencies were computed from Mie theory for 100 different particle sizes ranging from 0.1 to 5 microns. Note that the single scattering albedo, ϖ_0 , could also potentially introduce a separate wavelength dependence to τ_s ; however, any potential wavelength dependence would only be very weakly constrained by the observations since aerosols at any given height are only dominating the reflectance over small subsets of the entire spectrum. Preliminary retrievals showed that the weak dependence could be sufficiently accounted for by slight changes in scattering cross section alone.

Both single scattering and multiple scattering codes were tested for computing the model reflectance. In theory, single scattering calculations are sufficiently accurate for modeling reflectance from clouds and hazes with a total optical thickness less than

~0.1 (van de Hulst, 1957). In a cloud of greater optical thickness, the projected area of individual particles begins to overlap, and the resulting reflectance is not simply proportional to the number of particles. In these circumstances multiple scattering code is necessary for calculating the correct reflectance. Preliminary retrievals show that H-band scattering optical depths begins to exceed 1/10 at about 1.8 bars, suggesting multiple scattering occurs below this height. At these depths, the methane abundance is greater, and the increased path length of multiply scattered photons may potentially mitigate the contribution of multiply scattered light if the distances between scatterings are long enough; however, a simple test shows that doubling the scattering optical thickness of this layer produces a less-than twofold increase in reflectance, thus suggesting multiple scattering is indeed significant for the deeply penetrating regions of the H-band. To test the sensitivity, results from representative examples were retrieved using both single and multiple scattering calculations. Multiple scattering calculations require that individual scattering properties—bundled together in the above τ_s —be specified, since these properties are necessary for evaluating the contribution from subsequent scatterings. Figure 4 shows one example, demonstrating that the retrieved aerosol scattering optical depth for a deep cloud layer can be up to 45% less when using multiple scattering calculations, assuming the same conservative scattering phase function.

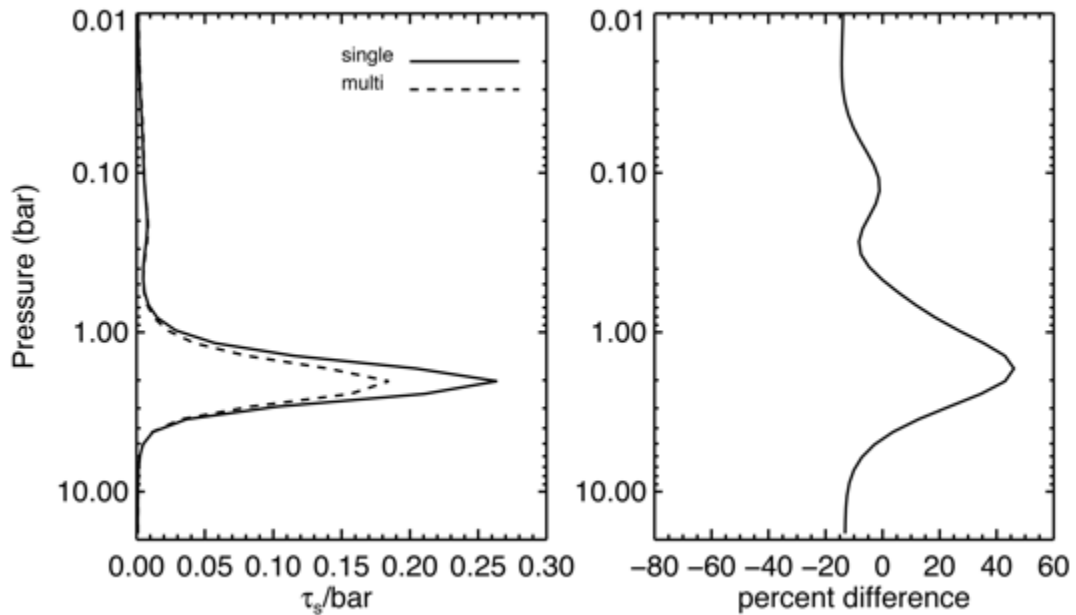


Figure 4. Comparison of retrievals from real data performed using both single and multiple scattering. Calculations assumed the same conservative scattering phase function. The plot on the left shows that less scattering optical depth is required to produce the same reflectance; the difference is most pronounced in the optically thickest cloud. The plot on the right shows the difference as a percentage of the multiple scattering results.

Different scattering assumptions can produce somewhat different results—e.g. a low single scattering albedo will more significantly reduce the intensity of the multiply scattered light as compared to the singly scattered light. So while multiple scattering calculations are potentially more accurate, uncertainties in the necessary scattering parameters still result in large uncertainties in the retrieved magnitude. For the present investigation, the value of knowing the aerosol distribution rests in the qualitative picture and relative changes as opposed to absolute values of retrieved parameters. Since the multiple scattering calculations are computationally very costly, the added computational time was deemed too burdensome given the uncertainties.

Hence, single scattering was assumed, and reported deep cloud scattering optical depths may be interpreted based on preferred scattering assumptions.

3.3 Retrieval Algorithm

Constrained vertical profiles of aerosol scattering optical depth and methane mole fraction were simultaneously retrieved from both H and K spectra using an inversion algorithm, also following Banfield et al (1996,1998) and Stam et al (2001). The method aimed to retrieve the simplest solutions possible while minimizing differences between observed and modeled spectra. Small perturbations to the modeled parameters at each height were used to compute the sensitivity of the modeled spectrum at each wavelength. Based on these linearized derivatives, an improved profile was computed through minimization of a modified quadratic merit function. Unlike the typical merit function that is minimized in least squares fitting, this modified function contained additional terms that constrained the solutions to lay close to reference values—in this case, the previously estimated values. The additional terms served to filter the solutions, preventing arbitrarily small changes in the modeled spectrum from mapping into spurious large changes in weakly constrained parameters. Assuming a correlation between adjacent layers imposed further restrictions on the profile. The profiles evolved iteratively, as new functional derivatives were computed each iteration to account for non-linearity in the solutions. More details on the retrieval algorithm formulation can be found in Section 2 of Conrath et al (1998).

Weights for the smoothness constraints and vertical correlations scales were optimized based on tests retrievals on synthetic data (described below) and the noise and information content of the real data.

3.3.1 Retrieval Uncertainties.

Retrievals of known profiles from forward modeled spectra with realistic noise were performed to refine the constraints and estimate the uncertainty in retrieved parameters. The synthetic retrieved quantities were subtracted from the true profiles for 250 cases and percent error was computed (see Figure 5). These ensemble tests suggest that retrieved values of $\tau_s \text{ bar}^{-1}$ were typically within 50% or better of the known profile given constraints placed on the methane profile. The methane mole fraction at the tropopause was on average accurate to within 60%, though occasionally retrieved values were off by a factor of two. While significant, these errors are less than the observed factor of four variance in the data. The retrieved methane values were typically greater than the true values at low pressures; this simply reflects the low information content of the data, which tended to keep solutions similar to the initial guess of a cold-trap limited methane profile.

At higher pressures, the methane abundance is fully fixed by the model assumptions, and the aerosols scattering optical depths must simply be chosen to produce the required, strong signal in the H-band window. Hence, the uncertainty at these depths is mostly due to error in the assumed methane abundance and absorption coefficients. Below these heights, optical depths become large at all wavelengths; there is no information, and the model converges with the initial conditions.

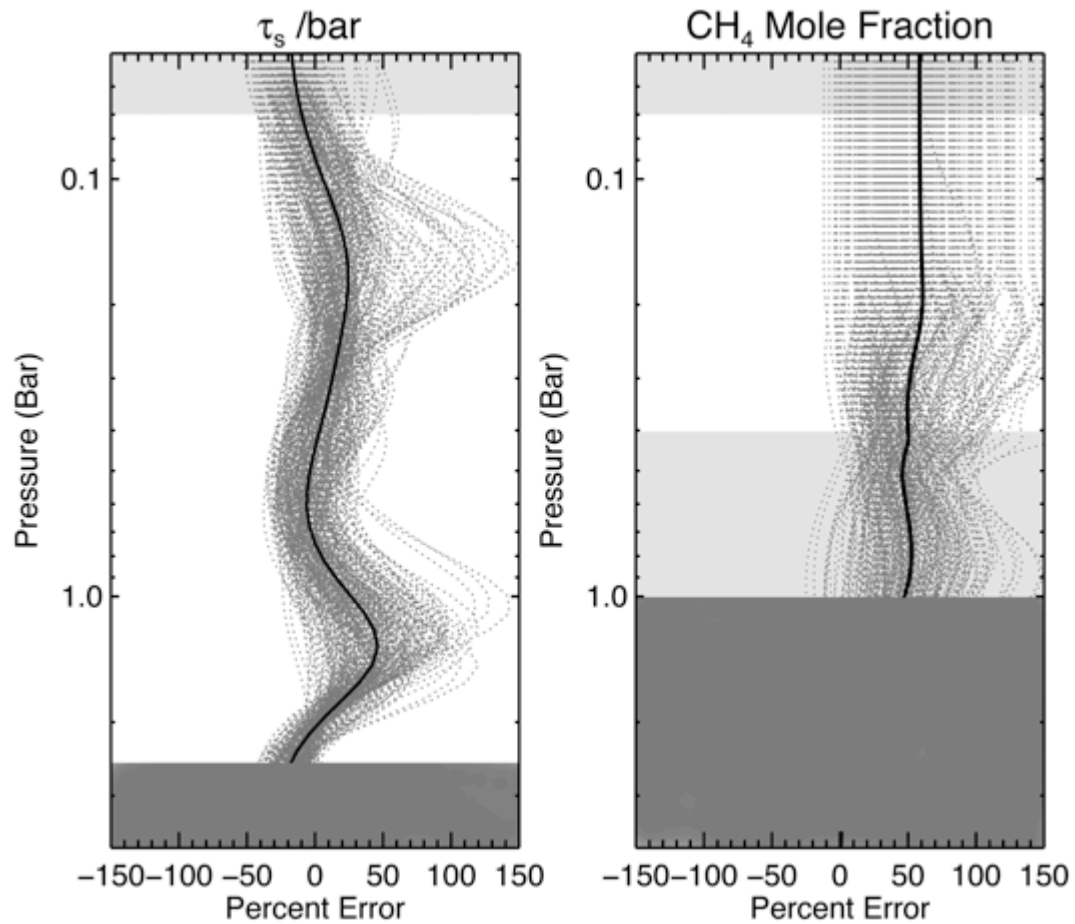


Figure 5. The difference between retrieved solutions to the vertical profiles and the true profiles that produced the spectra as a percentage of the true profiles. The plots show the result of 250 retrievals, with the mean value in black. The shaded regions once again show where the data content diminishes and results are strongly dependent on the initial conditions and assumed profiles.

The smoothness constraints imposed on the profiles limit the amount of vertical structure that could be retrieved in hypothetical cases. While sufficiently detailed for modeling the observations, the smooth profiles would fail to capture complex structure on lengths scales less than about a scale height. Discrete clouds emerge as broad extended peaks centered within roughly 25% of the same height.

The uncertainty in the retrievals depends on the amount of aerosol present. In particular, constraints of the methane mole fraction required sufficient aerosol abundance above 300 mbar in test profiles; if aerosol scattering optical depths per bar were below $10^{-3} \tau_s \text{ bar}^{-1}$, their aerosols provided insufficient reflectance for constraining the methane mole fraction. Observations in the hydrogen-dominated regions of the K-band suggest hazes exceeded this minimum requirement.

4. Results

4.1 Mean Results

Using the above methods, scattering optical depths and methane mole fractions were retrieved as a function of pressure and latitude for each observation in the data set. Scattering optical depths were expressed as $\tau_s \text{ bar}^{-1}$ at 1.48 μm . Over time and latitude, the vertical profiles of aerosols consistently displayed two distinct layers: an optically very thin haze near the tropopause and a deeper, thicker haze or cloud layer. This is consistent with result of other NIR spectral studies (e.g. Irwin et al. 2010; Tice et al., 2013). Table 2 shows mean values of retrieved parameters for each observation.

Observation	Upper Aerosol Layer Peak				Lower Aerosol Layer Peak				CH ₄ Mole Fraction	
	τ_s bar ⁻¹		Pressure (bar)		τ_s bar ⁻¹		Pressure (bar)		@100 mbar	
Date	Mean	Stddev	Mean	Stddev	Mean	Stddev	Mean	Stddev	Mean	Stddev
2001 Sep 3	9.39E-3	1.2E-3	0.218	0.018	0.291	0.064	2.51	0.25	1.15E-5	2.3E-6
2001 Sep 4	1.03E-2	1.1E-3	0.310	0.014	0.299	0.065	2.27	0.20	5.62E-6	1.2E-6
2001 All	9.85E-3	6.4E-4	0.264	0.065	0.295	0.005	2.39	0.17	8.6E-6	4.1E-6
2002 Aug 24	1.11E-2	2.8E-3	0.130	0.045	0.159	0.076	2.23	0.27	1.98E-5	2.4E-6
2002 Aug 24	1.06E-2	2.5E-3	0.115	0.038	0.161	0.081	2.41	0.31	1.83E-5	2.9E-6
2002 Aug 25	1.13E-2	2.7E-3	0.125	0.043	0.164	0.082	2.18	0.29	2.09E-5	3.4E-6
2002 Aug 26	1.07E-2	2.5E-3	0.109	0.039	0.164	0.074	2.29	0.27	1.94E-5	2.3E-6
2002 Aug 26	1.25E-2	3.7E-3	0.137	0.042	0.151	0.067	2.29	0.29	2.56E-5	7.9E-6
2002 All	1.13E-2	7.5E-4	0.123	0.012	0.160	0.006	2.28	0.09	2.08E-5	0.29E-5
2004 Jul 25	8.37E-3	1.5E-3	0.173	0.050	0.135	0.062	2.10	0.26	2.88E-5	4.3E-6
2004 Jul 25	9.44E-3	2.6E-3	0.127	0.036	0.142	0.060	1.94	0.21	4.51E-5	8.9E-6
2004 Jul 25	1.17E-2	3.4E-3	0.120	0.033	0.118	0.049	2.13	0.25	2.97E-5	5.5E-6
2004 Jul 25	9.65E-3	2.9E-3	0.117	0.032	0.109	0.046	2.05	0.19	3.89E-5	5.8E-6
2004 All	9.80E-3	1.4E-3	0.134	0.026	0.126	0.015	2.05	0.09	3.56E-5	0.78E-5
2005 Sep 16	1.09E-2	3.3E-3	0.117	0.027	0.138	0.056	2.10	0.22	5.93E-5	1.3E-5
2005 Sep 16	1.13E-2	2.2E-3	0.144	0.043	0.145	0.061	1.91	0.21	3.94E-5	6.0E-6
2005 Sep 16	1.03E-2	2.3E-3	0.135	0.037	0.158	0.066	2.07	0.20	4.22E-5	1.4E-5
2005 Sep 16	1.31E-2	3.5E-3	0.128	0.033	0.164	0.067	1.90	0.17	4.32E-5	5.5E-6
2005 All	1.14E-2	1.2E-3	0.131	0.011	0.151	0.012	1.99	0.11	4.60E-5	0.90E-5
2007 Aug 15	7.73E-3	1.2E-3	0.183	0.025	0.090	0.029	2.15	0.18	1.74E-5	4.1E-6
2007 Aug 15	7.46E-3	1.5E-3	0.149	0.046	0.115	0.041	2.17	0.19	3.23E-5	1.2E-5
2007 Aug 17	8.57E-3	5.4E-3	0.205	0.043	0.085	0.031	1.98	0.16	2.50E-5	6.4E-6
2007 Aug 17	9.03E-3	4.4E-3	0.226	0.020	0.081	0.031	1.87	0.17	1.26E-5	3.3E-6
2007 Aug 17	8.59E-3	1.7E-3	0.146	0.024	0.084	0.029	1.82	0.15	2.46E-5	8.5E-6
2007 All	8.28E-3	6.6E-4	0.182	0.035	0.091	0.014	2.00	0.12	2.24E-5	0.75E-5

Table 2. Disk- and yearly-averaged retrieved values.

The upper layer had a mean scattering optical depth of roughly $1.0 \times 10^{-2} \tau_s$ /bar with a peak height varying between 260 mbar and 120 mbar over the observed times. The total scattering optical depth above 500 mbar was $3 \times 10^{-3} \tau_s$.

The lower layer had an average scattering optical depth of $1.4 \times 10^{-1} \tau_s \text{ bar}^{-1}$ centered at a height of roughly 2.14 bars, with an uncertainty of roughly 25%. The height and reflectance of this layer steadily changed over the observed period. The scattering optical depth and central pressure decreased from means of $0.30 \tau_s \text{ bar}^{-1}$ and 2.39 bars in 2001 to means $0.09 \tau_s \text{ bar}^{-1}$ and 2.00 bars in 2007. The yearly averaged profiles of scattering optical depth are shown in Figure 6.

Sensitivity to the aerosol wavelength-dependent extinction efficiency was limited. The deeper cloud layers contribute the greatest reflectance in H band, but only over a relatively small window around $1.6 \mu\text{m}$, hence there is little information on how reflectance varies with wavelength. The K-band and strong absorption features of the H-band offer sensitivity to heights near the tropopause over a broader range of wavelengths. The data were best fit using a relatively flat dependence with only slight decrease towards longer wavelengths. Assuming Mie theory applies, this corresponded to scattering aerosols with a mean effective radius of roughly one micron or greater at pressures of a few hundred millibars. Particles much smaller than this produced less scattering at longer wavelengths (relative to shorter wavelengths) and proved marginally less compatible with data. This is roughly consistent with the wavelength dependence suggested by Irwin et al (2015), which drops quickly between 0.8 and $1.2 \mu\text{m}$ before slowly decaying towards longer wavelengths.

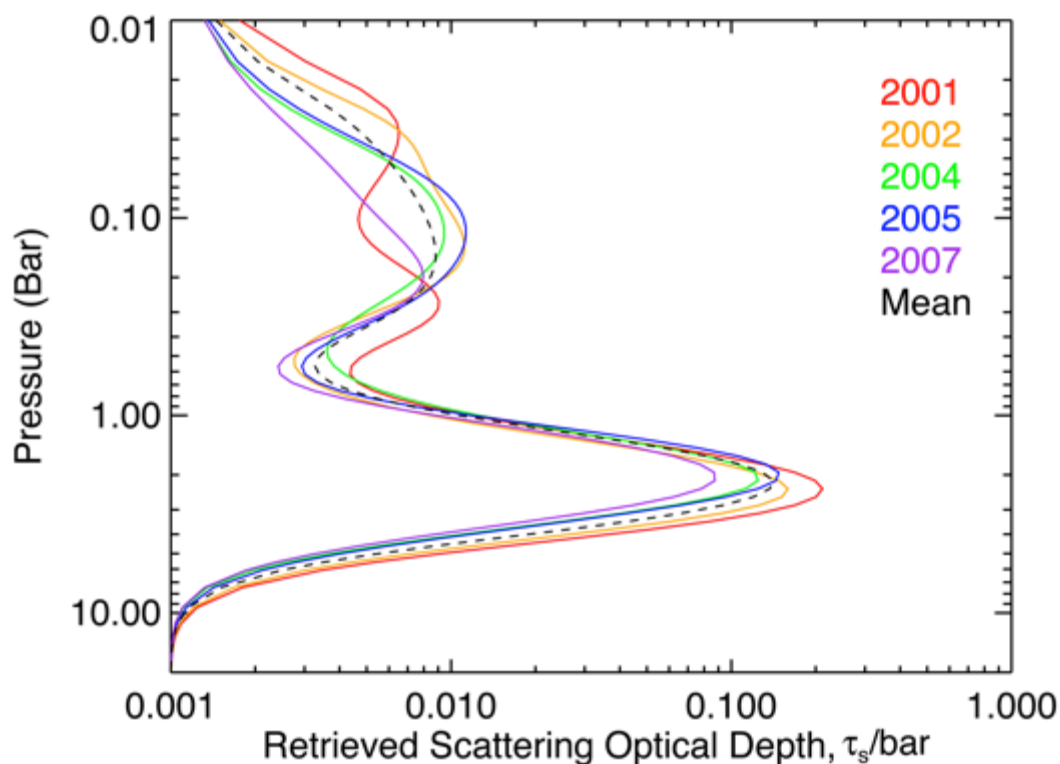


Figure 6. Yearly averaged profiles of aerosol scattering depth as a function of height. Years are designated by color, and the mean is shown in black (dashed line). Variation in the upper layer is within the uncertainties, while the deeper layer shows a significant trend of diminishing τ_s /bar over the 2001-2007 period.

In the lower stratosphere, the methane mole fraction was modeled as a uniform value extending up from the tropopause minimum. The retrieved mole fraction at 100 mbar had a mean value of $(2.7 \pm 1.6) \times 10^{-5}$. The retrieved 100 mbar methane mole fractions are very consistent with results from the Orton et al. 2014 modeling based on 2007 Spitzer Infrared observations; in that study, the authors reported a tropopause mole fraction of $(1.6 + 0.2/-0.1) \times 10^{-5}$ assuming a uniform eddy diffusion coefficient, K_{zz} , and $(2.5 + 0.3/-0.2) \times 10^{-5}$ assuming a sloped K_{zz} . The retrieved results therefore

favor the sloped eddy diffusion profile, but the errors bars are just large enough to permit both values. Yearly averaged profiles are shown in Figure 7.

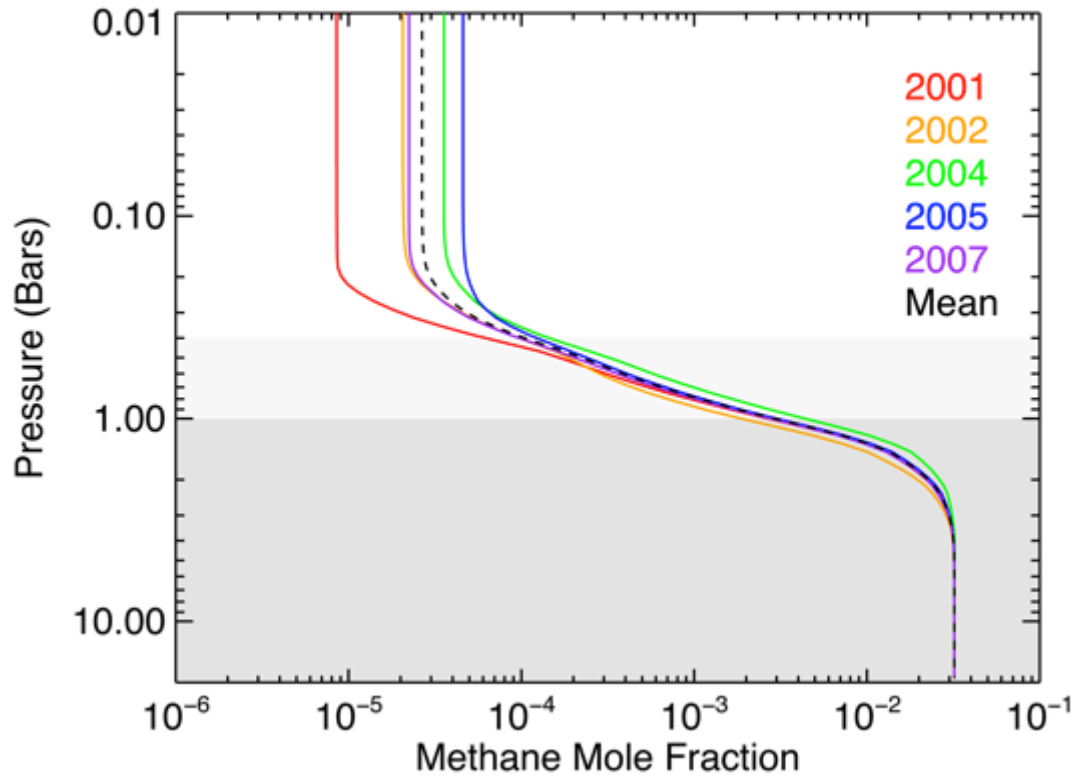


Figure 7. Yearly averaged profiles of methane mole fraction as a function of height. Years are designated by color, and the mean is shown in black (dashed line).

Different deep methane models were evaluated based on the goodness of the fits. Of the four different models tested, those with latitudinal variation provided the better fits. Models with a latitudinal dependence following Karkoschka and Tomasko (2011)—referred to as “case 3” above, with a fixed deep abundance of 3.2%, but with the height of this layer pushed deeper towards the poles—produced the lowest reduced-chi squares on average, though only marginally better than the “case 4” model following Sromovsky et al (2014) (See Figure 8). Indeed, the latter model produces very similar fits at most latitudes, and even marginally better fits at some northern

latitudes in 2007 data. Nonetheless, the 3.2% deep model of Karkoschka and Tomasko (2011) fit a majority of the data better and was thus adopted for all the retrievals.

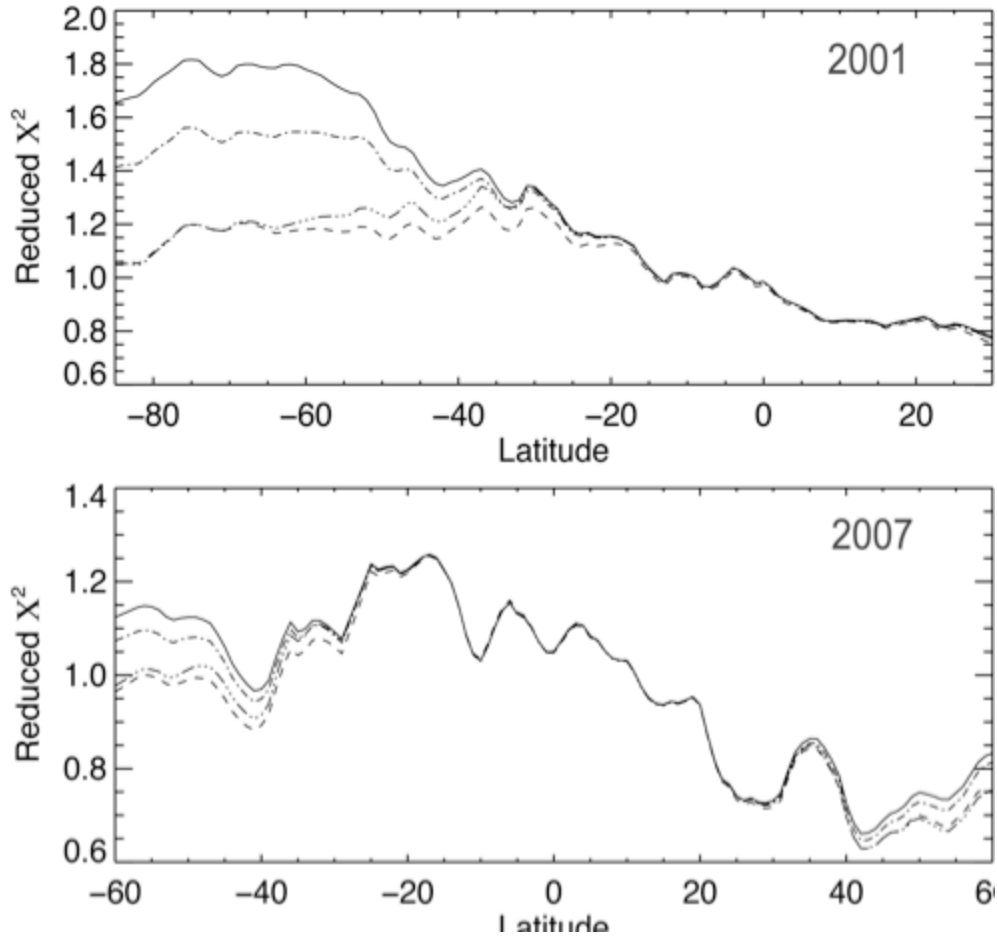


Figure 8. Goodness of fits plotted as a function of latitude for each of the four assumed models for the deep methane abundance. The results came from two different observations—the first from 2001 and the second from 2007. Reduced Chi squares were calculated based on the error between observed and modeled spectra for each latitude. Models correspond to Figure 3, with case 1 (solid), case 2 (dot-dash), case 3 (dashed), and case 4 (3x-dot-dash). Case 3, based on Karkoschka and Tomasko (2009) provided the best fits.

4.2. Latitudinal Variation

Retrieved aerosols scattering profiles were plotted as a function of pressure and latitude for each observation; the 100-mbar mole fraction of methane was plotted as a function of latitude. With the slit aligned roughly north-south at the central meridian,

these data provide meridional cross sections for given times and longitudes. Figure 9 shows examples from 2001 and 2007. Figure 10 illustrates scattering optical depths for the entire data set. The cross sections display significant trends in the lower layer scattering optical depth over latitude and time. The 2001 data shows greater scattering optical depths towards the southern latitudes, peaking around 50° S latitude, and decreasing towards the pole and northern hemisphere. The peak in aerosols corresponds to the latitude of the bright south polar collar. South of 45° S, where the assumed deep methane abundance profiles become deeper, the lower layer height gradually drops several hundred millibars. A deepening of the clouds pole-ward of 45°S was also previously noted in analysis of 2009 observation (Irwin et al., 2010). North of the equator, the τ_s bar⁻¹ drops by an order of magnitude. As the years progressed towards equinox, the aerosol scattering optical depths decreased in general, as shown in the mean profiles of Figure 6, but in particular, this change is most dramatic towards southern high latitudes. As the south polar collar diminishes, a northern equivalent appears to emerge by 2007. The results are a less reflective, somewhat more hemispherically symmetric cloud layer. These changes can be seen clearly in the total vertically integrated scattering optical depths shown in Fig. 11. Over the six year period, the total integrated scattering dropped by more than a factor of three at high southern latitudes and as much as a factor of five at the peak in the deconvolved data.

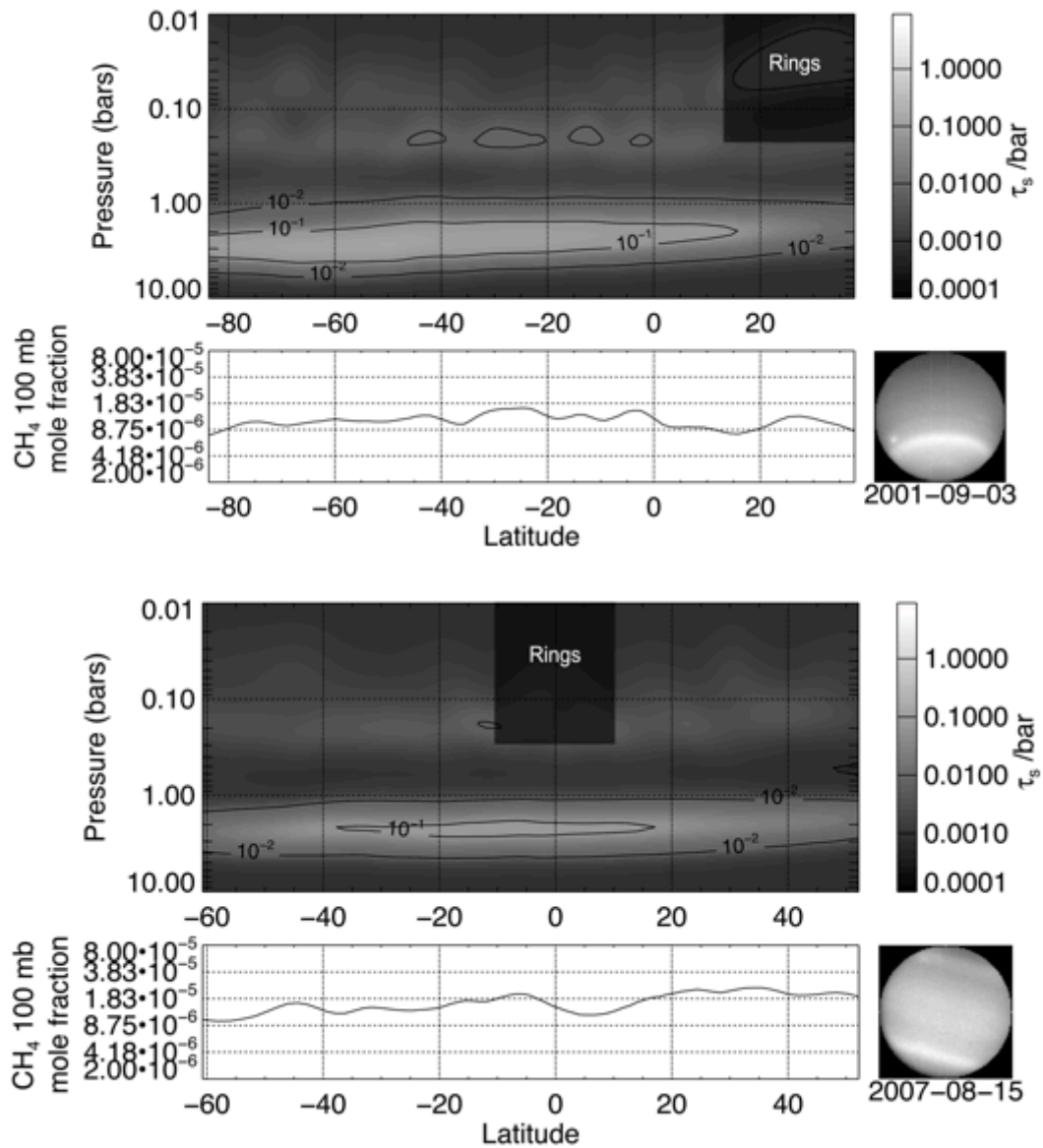


Figure 9. Retrieved aerosol scattering optical depths profiles and 100-mbar methane mole fractions as a function of latitude. (Top) Observation from September 3, 2001 showing prominent clouds near the southern pole (south is down in the image). (Bottom) 2007 observations showing reduced aerosol scattering and greater hemispheric symmetry. Regions dominated by the ring reflectance in the K-band are blacked out.

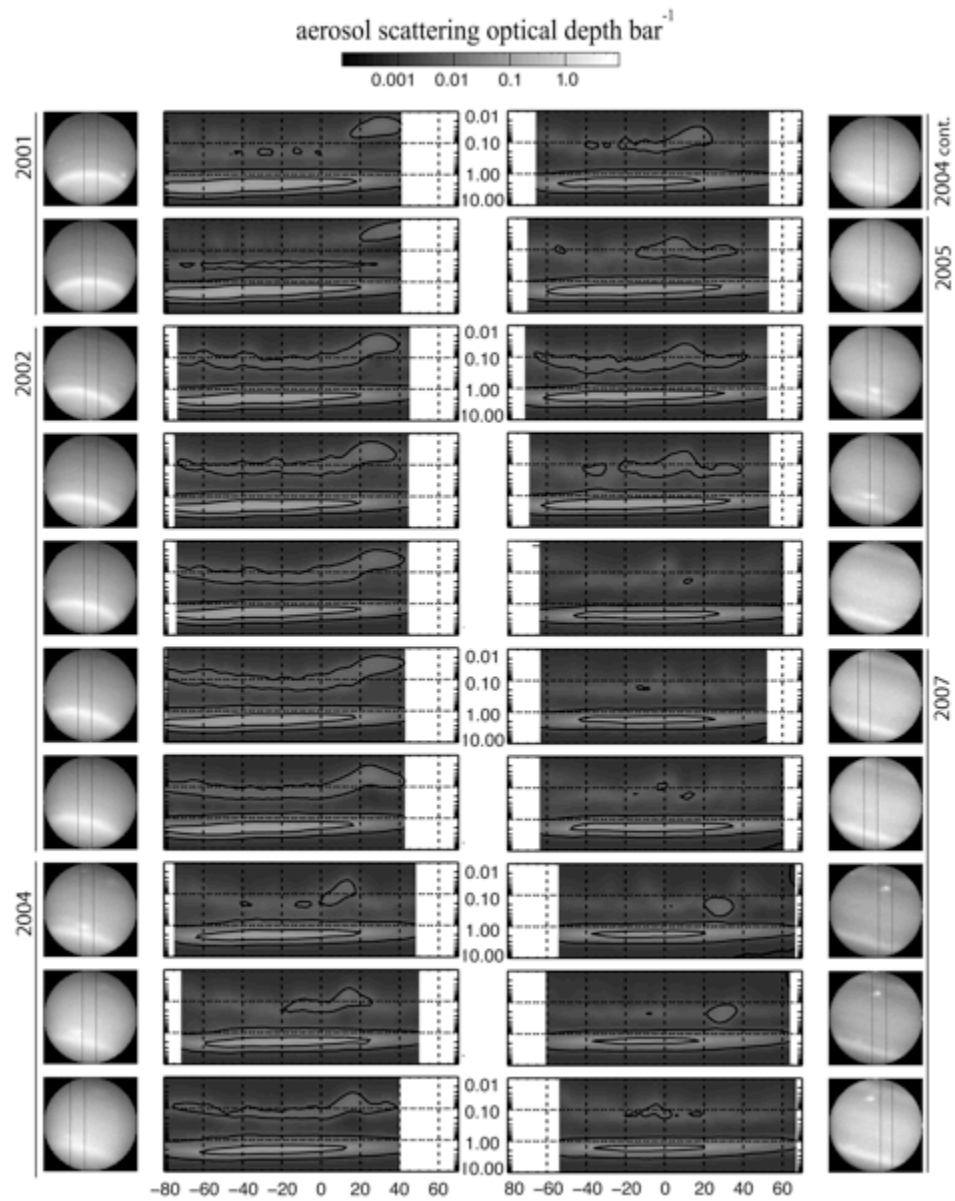


Figure 10. Aerosol scattering optical depth per unit pressure are plotted as function of pressure and latitude for all observations. South is down in the images. There is a significant reduction in the $\tau_s \text{ bar}^{-1}$ at all latitudes but particularly southern latitudes, resulting in a more symmetric pattern by 2007. Note that observations of Uranus' rings produce an artificial enhancement in $\tau_s \text{ bar}^{-1}$ as they move from 30°N to the equator over the 2001 to 2007 period.

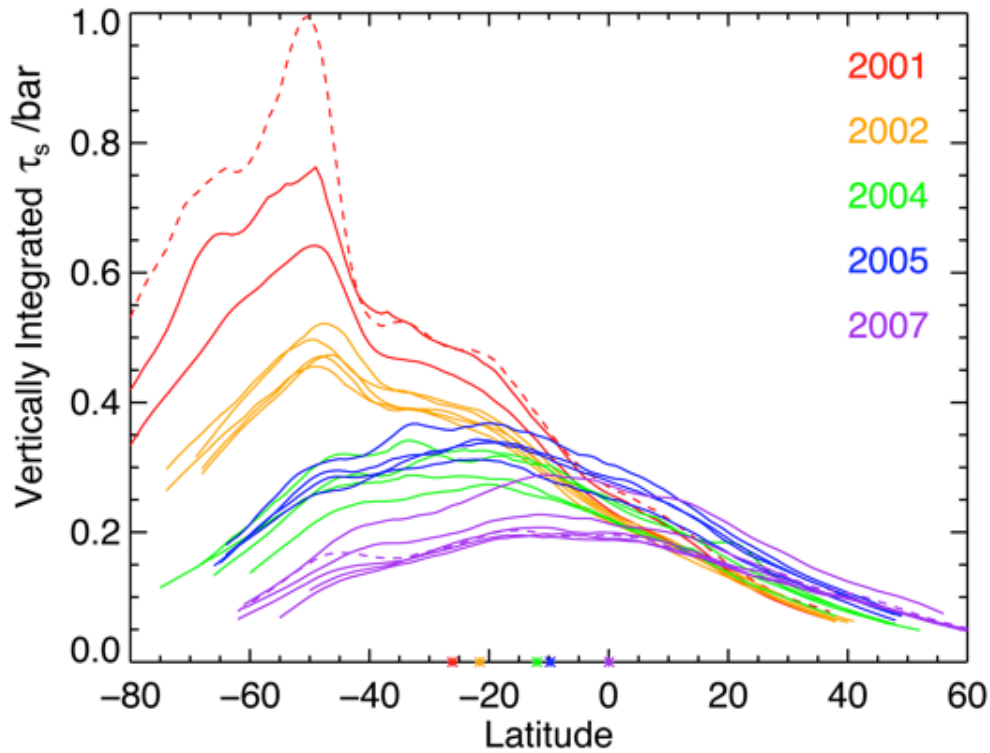


Figure 11. Vertically integrated scattering optical depths versus latitude for each of the observations, color-coded to indicate the year. The dashed lines represent the two cases in which the observations were deconvolved. Colored asterisks on the abscissa indicate the sub-solar latitude for each year. The data clearly shows a trend of diminishing scattering optical depth at southern latitudes progressing from 2001 to 2007. The trend is even more dramatic in the deconvolved data.

The tropopause methane mole fraction showed little obvious trend with latitude, but a slight trend over time. Figure 12 shows plots of the 100-mbar methane mole fraction for the data set. Though the error bars are large enough to account for much of the variation, the observations taken during any given year show consistency, even when taken over multiple nights as in the 2001, 2002, and 2007 observing runs. As also evident in the yearly mean values of Table 1, the retrieved 100-mbar methane mole fraction increases by a factor of roughly four from 2001 to 2005 before decreasing to just below the mean value in 2007.

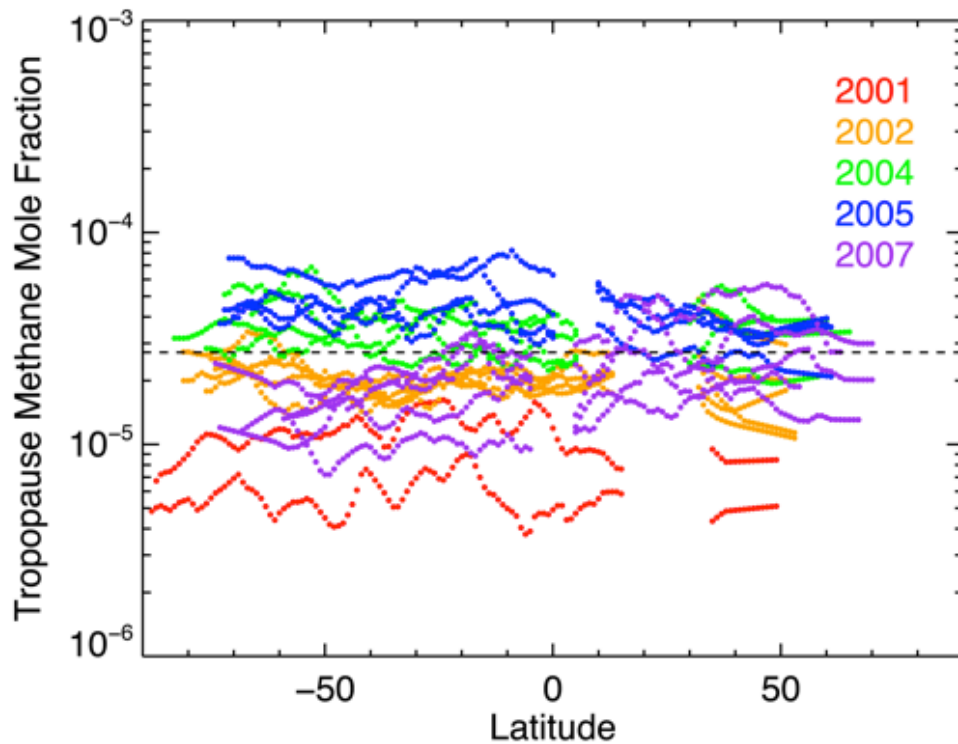


Figure 12. The retrieved methane mole fraction at 100 mbar (roughly representing the tropopause) plotted for each observation versus latitude, and color-coded to indicate the year. Though much of the variation can be accounted for by uncertainties in the measurements, clustering by year may suggest slight changes on yearly scales.

4.3 Lone Cloud Feature

Occasional discrete cloud features can be seen in the throughout the data. In addition to the consistent discrete feature that accompanied the south polar zone, a number of wispy clouds can be seen at mid-northern latitudes. The most prominent was observed on August 17, 2007 at rough 30° N latitude. The feature was roughly 10 pixels or ~6,000 km across (FWHM ~4,000 km) and is seen as increased reflectance in both H and K bands (see Figure 13). The extent of the feature is somewhat artificially exaggerated in due to limitations in atmospheric seeing and rotation of the disk, while the intensity of the light is potentially diminished by 5-10% as suggested by

deconvolutions of the point-spread function. Nonetheless, the feature reflectivity in the H-band was measured with an I/F of 0.0101—roughly 0.004 or 1.8 times brighter than nearby longitudes; for the K-band, the increase in I/F was $(1.6 \pm 0.4) \times 10^{-4}$. The K band increase is unique within the data and required the feature to have existed higher in the atmosphere than other clouds. Spectra were fortunately obtained for the feature and adjacent regions of the atmosphere. As Figure 14 shows, enhanced reflectance was observed at wavelengths corresponding to moderate to strong methane absorption features in the H-band as well as the near side of the K-band.

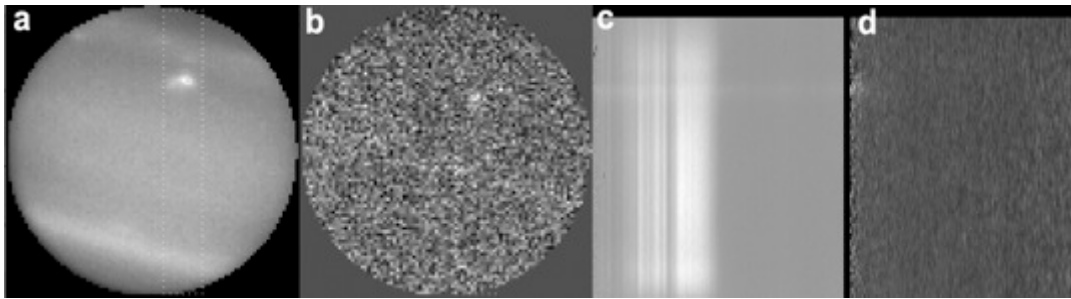


Figure 13. Images and compressed spectral images for the discrete cloud feature, as observed on August 17, 2007. The feature is seen as a bright spot just right of center in the upper half of the images. a) the H-band image, b) the K-band image, c) the H-band spectra, and d) the K-band spectra, showing just a hint of brightness on the left.

Retrievals reveal that the observed feature corresponds to an increased aerosol scattering optical depth centered at 240 ± 60 mbar. Vertical profiles show an enhancement of 0.029 ± 0.006 τ_s /bar relative to the surrounding atmosphere (Figure 15). Vertically integrated between 100 mb and 900 mb, the layer results in a 0.0073 ± 0.0015 increase in scattering optical depth relative to immediately adjacent locations. A full latitudinal cross section suggest the cloud may be seen as an enhancement in a more tenuous and uniform layer between 100 and 300 mb with no significant change in the 100-mbar methane mole fraction (Figure 16).

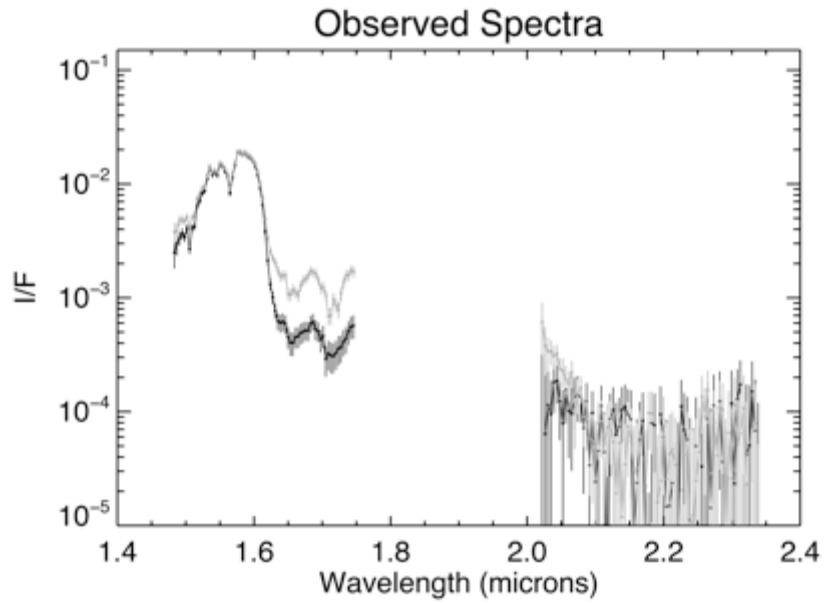


Figure 14. Spectra obtained for discrete cloud feature (gray) and adjacent longitude (black), along with error bars. Enhanced reflectance was observed at wavelengths corresponding to moderate to strong methane absorption features in the H-band as well as the hydrogen absorption in the near side of the K-band.

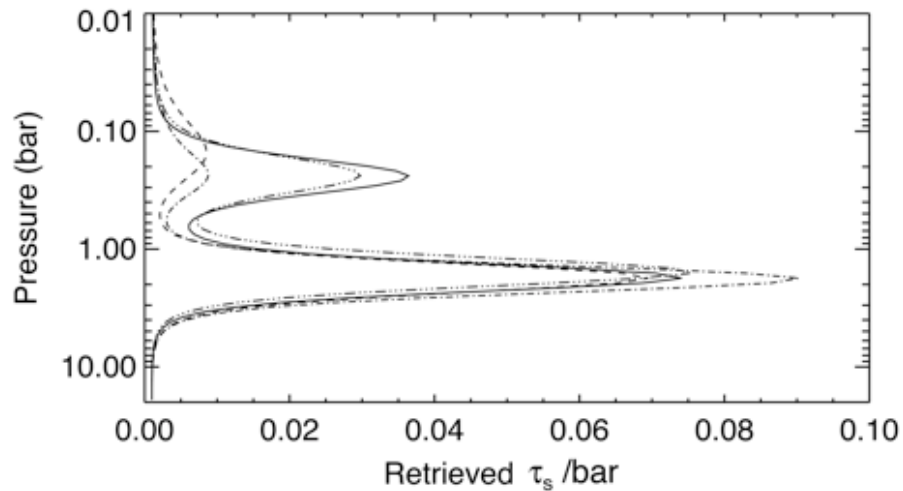


Figure 15. The retrieved vertical profiles of the scattering optical depth per bar as a function of pressure corresponding to the 30° N discrete cloud feature (solid line), a location just to its east (dashed line), a location just to its south (dashed-dot line), and the relative difference (3x-dot-dashed). The relative difference shows that the observed enhanced reflectance is due to an enhancement of aerosols centered at 240 mbar.

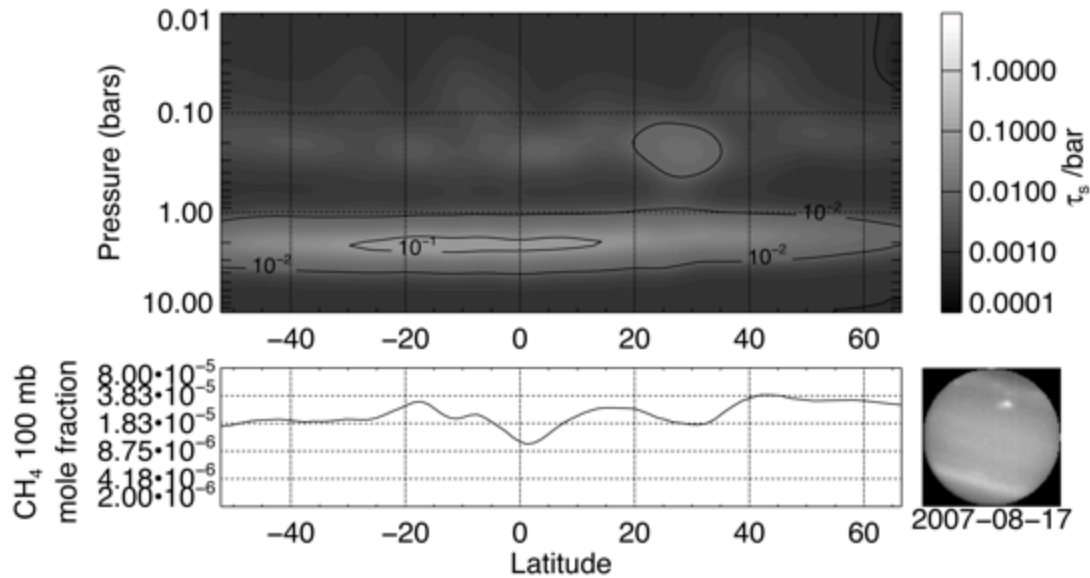


Figure 16. A latitudinal cross section including the bright cloud feature as an enhancement of aerosol scattering optical depth at 240 mbar and 30°N latitude.

5. Discussion

5.1 Cloud Structure and Seasonal Changes

The present study adds to a large number of studies that have examined cloud structure and seasonal changes on Uranus including near-IR spectra (e.g. Baines and Bergstralh, 1986; Sromovsky and Fry, 2007; Sromovsky et al., 2011; Irwin et al., 2009; Irwin et al 2010; Irwin et al., 2012a; Tice et al., 2013; Irwin et al., 2015 to name a few). The need for *at least* two vertical layers (either extended or thin sheets) is consistent with an overwhelming majority of these studies. The apparent relative minimum in aerosol scattering between the two layers found in the present retrievals is qualitatively similar to results found for Jupiter and Saturn (Banfield et al., 1998, Stam

et al., 2001). This may indicate a process of photochemical aerosol production in a stable layer below which aerosols are cleared by gravitational fallout, as explored by Banfield et al., (1998) or simply evaporated and diluted below the source.

Though inferred in a majority of near IR studies, the roughly 2-3 bar pressure of the deeper cloud layer is at odds with the 1.2 bar height inferred from Voyager Radio occultation analysis (Lindal et al. 1987). This discrepancy was thoroughly investigated by Sromovsky et al., (2011), who concluded that most modelers were assuming deficient methane mixing ratios—which moved the clouds deeper—and that the lower layer may be composed of multiple layers—namely a very thin 1.2 bar methane cloud and a deeper hydrogen sulfide cloud—lumped together in retrievals. By retrieving tropopause methane abundance, the former concern may be somewhat mitigated, but the potential of failing to resolve multiple layers spaced by roughly a scale height is still completely possible. Whether this layer is composed of a single convective condensate cloud layer, multiple condensate cloud layers, or a semi-infinite haze it is beyond the constraints of this present data and analysis; however, the changes in its properties over latitude and time may provide insight into its nature.

The deepening of the clouds pole-ward of 45°S, as seen in the 2001-2004 retrievals and noted in the analysis of 2009 observations (Irwin et al., 2010), may be interpreted as a latitudinal transition in the cloud structure and atmospheric circulation. The retrieved distribution is consistent with the circulation speculated by Sromovsky et al., (2014) with three layers of circulation cells leading to different cloud layers at different heights and latitudes; in this model, a roughly 1 bar methane cloud forms at the equator and extend 45° north and south; below this layer, a 1.5 bar hydrogen

sulfide cloud exists at mid-latitudes in the upwelling branch of a deeper circulation cell. Though the retrieved heights are somewhat deeper, the qualitative picture may apply—the change in height at 45° may be where the methane cloud ceases, leaving the deeper H_2S cloud exposed. The bright zone or “polar collar” is presumably the optically thickest part of this H_2S cloud, and its reflectance is somewhat enhanced by the lessening cloud-level methane mole fraction at these latitudes. Interestingly, microwave observations also suggest a transition in opacity at 45° at much greater depths (Hofstadter and Butler, 2003); this transition increased in intensity following the previous solstice. A third, deeper circulation layer with an ammonium hydrosulfide cloud is invoked in the Sromovsky et al. (2014) model to explain these observations.

The dramatic change in the reflectance and total scattering optical depth from 2001 to 2007 (see Figure 11) is consistent with other studies using observations covering different periods between 2004 and 2011 (Irwin et al., 2009, 2010, 2012; Sromovsky et al., 2009). The retrievals show that the observed trend is due to changes at the ~ 2 bar layer.

The scattering phase angle changed by less than a degree between 2001 and 2007, so the observed changes are truly intrinsic changes in the particle scattering properties, the assumed methane abundance, or the aerosol abundance. Since τ_s is a product of the scattering parameters, the observed change in reflectance may potentially be due to changes in any of its component factors. The scattering phase angle or single scattering albedos may potentially change with changing particle sizes or aerosol chemistry; while the data showed no significant change in the extinction

efficiency behavior and related particle size, only a small range in wavelengths were sensitive to the 2 bar cloud layer. Temporal changes in the single scattering albedo are also possible.

Such rapid response in the aerosol abundance due to seasonal changes is surprising given the potentially long radiative and dynamical timescales. Conrath et al., (1998) suggested radiative and dynamical time constants of 130 and 700 years at 300 mbar based on temperature and para-hydrogen fields inferred from Voyager IRIS observations. Dynamical time scales are presumably shorter in deeper, convective regions of the atmosphere. The reduced optical thickness may be a result of weakening vertical velocity associated with upwelling in the southern hemisphere. In context of the circulation model discussed above, this would be most directly attributed to weakening of the mid-level circulation cell associated and associated hydrogen sulfide cloud.

Alternatively, the rapid response may suggest a direct insolation or photochemical component. Studies of Saturn's atmosphere have shown that the hazes have clear seasonal trends. Pérez-Hoyos et al., (2005) noted that optical thicknesses of Saturn's stratospheric hazes at visual wavelengths increased with increasing insolation, which makes sense if photochemical production was the source; however, the deep tropospheric hazes *decreased* with increasing insolation (Pérez-Hoyos et al., 2005). Conversely At 5 μm , the tropospheric haze and clouds appear optically thicker in the summer hemisphere (Fletcher et al., 2011). In Saturn's case, the explanation has been attributed to increases in the particle size and the relative extinction efficiencies. Particle sizes were found to be larger in the summer than the winter hemisphere by a

factor of 2 to 4 ((Karkoschka and Tomasko, 2005). In the case of Uranus, a change in effective mean particle sizes may largely explain the significant change in aerosol scattering optical depth at 1.48 microns with little to no seasonal lag. For example, a factor of five reduction in the scattering extinction efficiency could be accomplished by reducing the scattering size parameter, $2\pi a/\lambda$ (where a is the effective mean particle radius), from 6 to 2 in a cloud with an effective size variance of 0.1 or less (Hansen and Travis, 1974). At 1.48 μm , this translates to a change in particle radius from about 1.4 μm to 0.5 μm . Irwin et al (2015) reported a particle size of $0.86 \pm 0.04 \mu\text{m}$ at the 2 bar level in analysis of 2009 observations, but most modelers have assumed particles were roughly 1 μm in radius in the past due to the poor leverage afforded in the narrow deeply penetrating passbands. Note, however, that changes in the particle size alone would be expected to change the extinction efficiency and reflectance at other wavelengths. The change proposed above would lead to a slight increase in scattering optical depth in visible wavelengths, which is inconsistent with the slight, gradual slight darkening observed in southern latitudes over the late 1990s (Rages, 2000; Karkoschka, 2001); however, comparisons between wavelengths may also be complicated by changes in normalized scattering phase function and single scattering albedo. It remains possible that a change in particle size and scattering properties could easily contribute to the observed seasonal changes.

5.2 Discrete Cloud Formation

Several observers have noted discrete cloud features on Uranus over the past decades. Eight discrete clouds were seen in Voyager images (Smith et al. 1986), and Karkoschka (1998, 2001) summarized activity including several dozen spots between 1994 and 2000 seen in HST images. A number of particularly bright clouds have been observed at mid-Northern latitudes in 1999, 2004, 2005, 2007, 2011, and 2014 (Sromovsky et al. 2000; Sromovsky and Fry, 2004; Sromovsky et al., 2007; de Pater et al., 2014). A majority of the brightest clouds were observed around 30° N and appeared to persist on timescales of at least days and possible years. The August 2005 feature was the brightest observed up to that time, and was centered at 30.2°N (Sromovsky et al., 2007). Observations a year later showed features at roughly the same latitude, but they also revealed an accompanying dark spot. June 6, 2007 Keck II images (Sromovsky et al., 2009, 2012) once again showed a bright complex at roughly the same latitude apparently associated with a dark spot. Sromovsky et al., (2009) analyzed the 2007 bright feature's motions and found slight oscillations in latitude and longitude. The August 17 2007 feature presented here is likely the same complex observed five weeks later.

Radiative transfer analysis showed that some of these clouds reached heights of roughly 500 to 350 mbar (Sromovsky et al., 2007). At these heights, the atmosphere is very stable to convection. Aerosols could potentially be lofted to these heights through deep convection if updrafts are sufficiently energetic to overcome the stability (e.g. Lunine and Hunten, 1989; Stoker and Toon, 1989). Such convection would have to originate at great depths where condensation of water and other deep

constituents can contribute to latent heating and drying of the parcel. With positive buoyancy, the parcel would then need to accumulate enough kinetic energy over its ascent to overcome the large stability at above the ~ 1 bar level. The parcel would also need to be very dry by the time it reaches the 300 mbar height in order to produce a number density of aerosols consistent with the observed scattering optical depths.

Alternatively, the cloud features could be formed by other means than convection. The apparent longevity, oscillatory motion, and accompanying dark spot suggest these clouds may be associated with vortex circulations. This would be akin to the bright companion clouds seen over the dark spot on Neptune in Voyager II images (Smith et al., 1989) and have been thought of as somewhat like terrestrial orographic clouds. Neptune's companion clouds have been modeled as flows along the surfaces of constant density (isentropic surfaces) rising over perturbations due to local temperature anomalies (Stratman et al., 2001). Clouds formed by this process should be very thin given the modest lift and low methane mixing ratios cloud heights. The retrieved optical thickness of this cloud can be used to help evaluate the consistency of the observations with formation models.

From the observed spectra, the retrieved optical thickness, τ_s , and vertical extent of the cloud were inferred. By approximating aerosols as spherical particles with scattering cross sections of $\sigma = \pi a^2 Q_s$, then optical thickness per unit area can be roughly converted to a mass per unit area:

$$M = 2 a \rho \tau_s / 3 \varpi_0 PF Q_s$$

Where M is the total aerosol mass per unit area, a is the effective particle radius, ρ is the particle density assumed, ϖ_0 is the single scattering albedo, PF is the normalized

scattering phase function, and Q_s is the scattering extinction efficiency. With $a \approx 1 \mu\text{m}$, the density taken to be $\rho \approx 0.5 \text{ g cm}^3$ for methane ice, $\omega_0 \approx 0.7$, a size appropriate phase function of $PF \approx 0.7$, and a scattering extinction efficiency of $Q_s \approx 2$, the retrieved total scattering optical for the layer, $\tau_s = 7.4 \times 10^{-3}$, yields a mass per unit area $M \approx 3 \times 10^{-3} \text{ g}$.

The total mass of condensate of the observed cloud can then be related to the amount of condensate expected by condensation of a rising parcels of atmosphere. Using a classical parcel theory description, the parcel begins with a given methane mixing ratio and temperature, typically taken to be equal to the surrounding ambient atmosphere; as it rises, the parcel does work on the surroundings and consequently cools as it loses energy. If the equilibrium vapor pressure of methane in the parcel exceeds the temperature dependent saturation vapor pressure, the excess vapor condenses out forming aerosol. The aerosol may then be left at the height it condensed (a pseudoadiabatic process) or taken along with the parcel (a reversible adiabatic process), or a combination of the two as is typical in terrestrial cases. Here it is assumed that the aerosol is pseudoadiabatically left behind for simplicity, but given the meager vertical distances and mass condensate, the choice of process is inconsequential to the result. The buoyancy of the parcel can be evaluated at each step of its rise, and the energy required or released by the ascent can be tallied. Additionally, complications can be added by including entrainment and supersaturation; for these calculations, entrainment is parameterized following Stoker and Toon (1989) and condensation is delayed to allow a supersaturation of 5% based on terrestrial values.

This process can be plotted using a classic thermodynamic diagram as shown in Figure 17. The retrievals place constraints on the cloud height, total aerosol mass per unit area of condensate, and the methane relative humidity of the environment. Through the simplified thermodynamics of parcel theory, these retrieved parameters translate to constraints upon the initial conditions of the parcel. If the parcel is assumed to have an initial methane abundance and temperature set by the retrieved methane profile and assumed temperature profile, then the condensation height is unique to a certain starting pressure. With the many given assumptions, the condensation at the retrieved 240 mbar central peak of the 2007 cloud feature would require the parcel to have begun its ascent at 322 mbar. The amount of condensate produced depends on how far the parcel is lifted. To be self-consistent with the values inferred from the retrievals, the parcel would have to rise to 236 mbar in order to condense roughly 3×10^{-3} g per unit area; this 86 mbar change equates to roughly 1/3 of a pressure scale height ($H \sim 21.77$ km) and a temperature drop of 6.0 K. The atmosphere is stable at this height, so lift across a vertical density gradient would require ~ 34 J of energy per kilogram of atmosphere, which equates to an updraft speed of ~ 8 m sec^{-1} . Alternatively, if parcel is thought to move along a sloped isentropic surface, this suggests that the anticyclone would have a horizontal temperature gradient comparable to the temperature drop (~ 6.0 K). Smaller temperature drops can be accommodated if the parcel begins with a slightly greater methane mole fraction and at a slightly lower pressure. For comparison, the EPIC modeling of Neptune's companion clouds by Stratman et al. (2001) found that those clouds were best reproduced with a typical pressure drop of 3 mbar from the 76 mbar

height, corresponding to half a kilometer, 4% of a scale height, and 1 K temperature drop. The difference could be explained by a relatively lower methane mixing ratio in the Uranus atmosphere, which requires a greater ascent prior to reaching condensation assuming. If the methane mole fraction were closer to saturation, the required ascent would be less. If the environment were assumed to be saturated in the above calculations, with no supersaturation necessary, the parcel would need to rise just 3 mbar—from 240 mb to 237 mb—which corresponds to roughly 0.3 km in height, ~1% of a pressure scale height, and a 0.05 K temperature drop—somewhat more consistent with the Neptune modeling results.

Similar analysis may be applied to penetrative deep convection, but solutions require extreme initial conditions. The deep atmosphere is much richer in methane than the stratosphere, and so the mass of condensates quickly becomes very large. In order to produce the aerosol mass and height inferred from the retrieved scattering optical depths while still achieving enough buoyant energy to penetrate the stable upper troposphere, the rising parcel would have to begin extremely dry and warm relative to its surroundings. For example, a parcel beginning its ascent at 1 bar would need to be roughly 3 K warmer and 3×10^{-3} dryer than the surrounding atmosphere in order to condense the same amount of aerosols at the observed heights. Conceivably, initial conditions could be more moderate if entrainment and mixing were much more vigorous than modeled here, but nevertheless, deep convection without significantly higher optical thickness appears unlikely. The retrieved scattering optical depths are thus more consistent with lift initiated near the observed cloud heights, as expected with companion clouds flowing over vortex circulations. With the retrieved methane

abundances and assumed scattering properties, the vortex would be forcing lift from roughly 320 mbar up to 230 mbar. While uncertainties in the parameters can produce a range of different values, the qualitative picture remains unchanged.

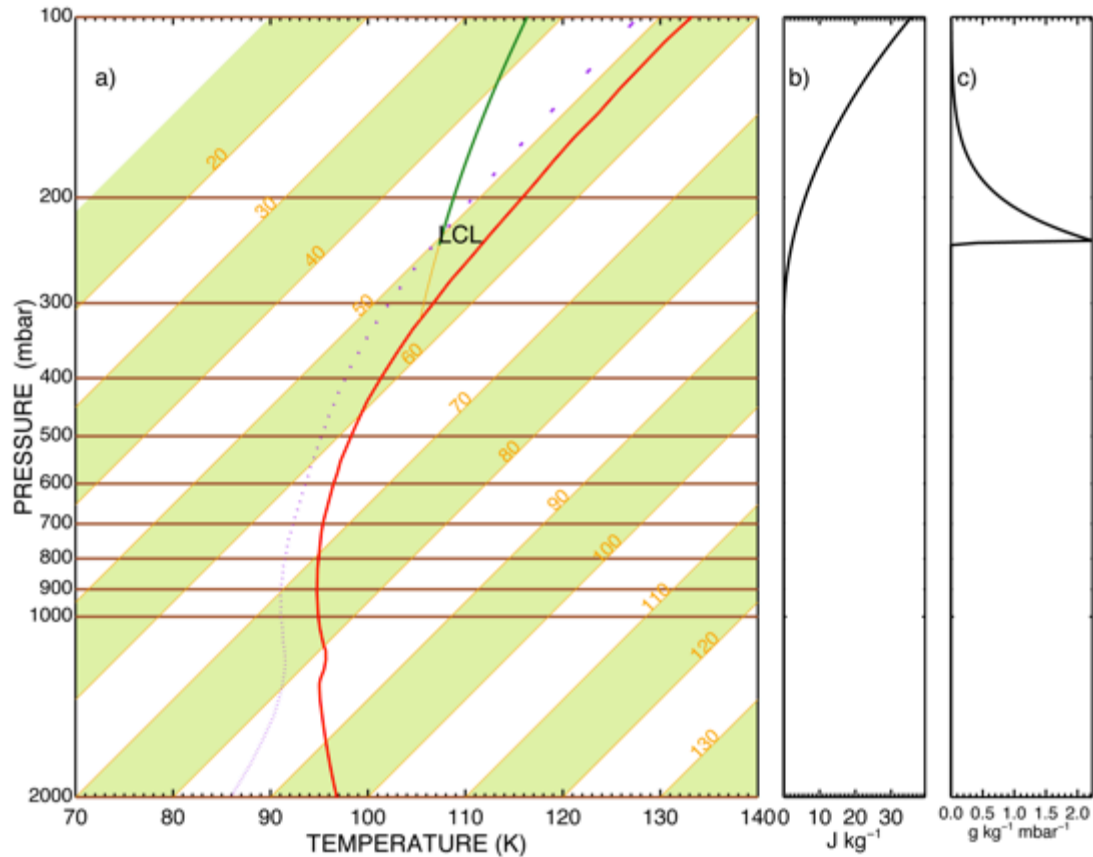


Figure 17. a) Thermodynamic diagram showing a hypothetical sounding for the Uranus atmosphere. Temperatures are skewed at a 45° angle, increasing down and to the right. Pressure is on the y-axis, increasing down. The red line represents the assumed temperature profile ('model F' of Lindal et al. 1987). A faint, purple dotted line represents the methane saturation temperature. The temperature of a parcel of air forced to ascend dry adiabatically from 315 mb is plotted in orange as it deviates from the ambient atmospheric profile; the line color becomes green when saturation occurs (marked LCL for Lifting Condensation Level) and the parcel rises wet pseudo-adiabatically. b) The amount of energy necessary to raise the negatively buoyant parcel (convective inhibition) per unit mass as a function of vertical pressure. c) The amount of condensate produced as a function of vertical pressure.

6. Concluding Summary

Spatially resolved, Near IR spectra of Uranus were analyzed to infer the atmospheric distribution of aerosols and methane.

Aerosol scattering optical depths showed two distinct layers—an optically very thin haze near the tropopause and a deeper, thicker haze or cloud layer. The lower layer peaked at a pressure of ~ 2.1 bars and exhibited changes in reflectance with latitude and time. Scattering optical depths were found to be greatest in the southern hemisphere, centered at $\sim 50^\circ$ S in 2001. From 2001 to 2007, the total scattering optical depth of the deeper layer diminished by a factor of three or more, particularly at southern summer latitudes, resulting in a more roughly symmetric distribution. This analysis adds to a limited but growing body of observations documenting temporal changes on Uranus.

The changes in reflectance from 2001 to 2007 appeared to be linked to seasonal change as Uranus arrived at equinox, suggesting insolation strongly affects the aerosol distribution. Given potentially long radiative and dynamical time scales, the relatively rapid changes may be attributed to changes in aerosol scattering properties, specifically modest reductions in particle size and scattering phase function; however, the present data cannot distinguish between several potentially changing scattering properties and potential changes in aerosol abundance. Future research utilizing center-to-limb analysis over a wide range of wavelengths will likely be needed to determine which factors contribute to the observed temporal changes.

The overall distributions of aerosols were consistent with—but not strongly discriminating among—speculative circulation models that include at least two layers of circulations cells at different latitudes and pressures. Such models may explain the change in cloud heights and reflectance seen at $\sim 45^\circ\text{S}$.

Best fits to the data were achieved with a methane distribution that decreased towards the poles, consistent with the findings of recent studies (Karkoschka and Tomasko, 2011) and circulation models with downwelling at the poles. The methane mole fraction at the tropopause was retrieved with an average value of $(2.7 \pm 1.6) \times 10^{-5}$, significantly below saturation and consistent with previous findings (Orton et al., 2014). No significant variations in latitude were detected, but a factor of four increase was noted from 2001 to 2005—larger than can be accounted for by estimated uncertainties. Potential temporal changes in the 100-mbar methane mole fractions have not been previously investigated and thus require additional study.

Finally, a discrete cloud feature of unusual height was analyzed. Despite the relative brightness, the cloud's observed reflectance, retrieved scattering optical depth, and inferred aerosol mass are very low. All together, the results favor the interpretation of this and similar cloud features as bright companion clouds associated with dark or unseen vortices.

The present study adds to a growing number of studies attempting to characterize the distribution of aerosols and methane in the atmosphere of Uranus. Using Earth based observations aided by adaptive optics, the novel approach taken above attempts to discriminate between potential cloud and haze formation dynamics using observations of reflectance, previous findings of the temperature and methane

profiles, and a series of assumptions made necessary by the lack of data. Stronger constraints on the methane distribution at the highest cloud levels are difficult given the very low aerosol optical depths and signal to noise ratio in the strongest methane bands. Uncertainties in the methane abundance would need to be an order of magnitude less to confidently characterize latitudinal variation at the tropopause. Likewise, greatly reduced uncertainties in the K-band reflectance would be needed to measure potential para-hydrogen disequilibrium and the circulation it implies. A better understanding of the dynamics and seasonal changes taking place will require continued spatially resolved observations over seasonal time-scales (i.e. decades) and at a range of wavelengths necessary to resolve ambiguities in the observed reflectance. Even so, the great distance and extreme axial tilt of Uranus limit our views from Earth. A designated spacecraft mission will ultimately be necessary in order to make significant advances in our understanding of the atmosphere and how it may change in time.

CHAPTER 2

AEROSOLS AND METHANE FROM NEAR-IR SPECTRA: NEPTUNE

1. Introduction

Though similar in size and composition to Uranus, the planet Neptune has displayed a significantly more dynamic atmosphere than its neighboring ice giant. Indeed, with prominently varying clouds likely carried by the fastest winds in the solar system, Neptune appears surprisingly energetic given its great distance from the Sun. Unlike Uranus, Neptune evidently has a larger internal heat source, which may likely help to explain the dynamic weather we observe.

For both planets, our first detailed views of the clouds came from Voyager II. While Uranus then appeared relatively muted, Neptune was marked with several distinct features, including a large, dark vortex, which swirled as rapidly changing, white clouds seemingly skirted far above. These whiter companion clouds were observed to change over hours, with a fixed position suggestive of terrestrial orographic clouds (Smith et al., 1989). These and other white clouds appeared to cast shadows down upon an indistinct, darker cloud deck below. Analysis indicated that these layers were vertically separated by some 50 km to 100 km—roughly two to four pressure scale heights.

Subsequent observations over the past decades from HST and ground based adaptive optics have shown bright, high clouds varying significantly in coverage on timescales of ~ 5 years (e.g. Karkoschka, 2011, Hammel et al, 1997, Sromovsky et al., 1995). The localized clouds of the Voyager days appear scarce when compared to the extended bands of white clouds seen in the spatially resolved ground-based images

taken a dozen years later. Spectra and filtered images sensitive to different atmospheric heights have confirmed the rarified heights of these highest clouds, with some at or above the 100 mbar tropopause (Sromovsky et al., 2002; Gibbard et al., 2003), far higher than the ~ 1 bar height expected from simple thermochemical models for methane (de Pater et al., 1991), but lower than the expected height of photolytic ethane and acetylene hazes. Clouds in the northern winter hemisphere were found to be higher yet—up 40 mbar, well within the lower stratosphere. The presence of variable clouds at these stably stratified heights raises intriguing questions regarding their formation. Are these related to vortices, and what could cause the half-decadal changes in high cloud coverage? If composed of methane, what can this tell us about the vertical distribution of methane and the general circulation?

Observations suggest the methane abundance in the lower stratosphere is greater than expected given the temperature structure. Inferred temperature profiles show a tropopause minimum of less than 59K (Lindal, et al., 1990; Conrath et al., 1991; Fletcher et al, 2014). With methane sourced from below, the minimum temperature should effectively limit the methane abundance by the corresponding saturation vapor pressure, hence serving as a cold trap. By this reasoning, the methane abundance should not increase with height beyond the cold trap value. Nonetheless, observations suggest methane values in the lower stratosphere in excess of the cold trap saturation vapor pressure (Orton, et al., 2007, Fletcher et al., 2010). Explanations for this enhanced stratospheric methane have included convective penetration (Hunten, 1974; Stoker, 1987; Lunine and Hunten, 1989), seepage through anomalously warm polar regions (Orton, et al, 2007) and strong upwelling through a

broad tropopause (Conrath et al., 1998; Karkoschka and Tomasko, 2011; dePater et al., 2014). Measurements of latitudinal and temporal variations in the methane abundance may help constrain these different theories, perhaps providing insight into the mechanisms that produce the differences in appearance between Neptune and Uranus.

In the present study, near-infrared (NIR) spectral data of Neptune covering a period from 2001 to 2007 are investigated following techniques similarly applied to Uranus observations of the previous chapter. Using a radiative transfer inversion algorithm, the vertical distribution of clouds, hazes, and methane are retrieved over a range of latitudes. Latitudinal and temporal variations are reported, while cloud properties are analyzed in context of formation mechanisms. Section 2 describes the data set, followed by the analysis techniques in section 3, and results in section 4. Section 5 presents a discussion of the results, concluding with a summary in section 6.

2. Data

Observations of Neptune were made annually between 2001 and 2007 at the Palomar Observatory, using the 200-inch (5.1m) Hale Telescope and the Palomar High Angular Resolution Observer (PHARO) near-infrared spectrograph and adaptive optics (AO) camera system (Hayward, 2001). The PHARO instrument captured spatially resolved images and spectra in both the H (1.487-1.783 μm) and K (2.028-2.364 μm) bands. The spectrograph slit was aligned with such that observations provided independent spectra for a range of latitudes.

The data were obtained as part of a seasonal monitoring campaign by Don Banfield and colleagues. Annual observing runs, each covering one to three nights,

sampled Neptune at several longitudes in the years surrounding the 2005 Neptune summer solstice. Overall, 27 observations were included in this analysis, with dates and times listed in Table 1. Data from 2005 were not included due to poor AO performance and poor weather. Phase angles for all data ranged between 0.2° and $.8^\circ$.

Table 1. Observations Dates, Times (UTC)

(year-month-day, hr:mn)

2001-09-01, 05:19
2001-09-01, 05:29
2001-09-02, 05:55
2001-09-04, 05:51
2002-08-24, 06:49
2002-08-24, 07:03
2002-08-25, 07:25
2002-08-25, 06:59
2002-08-26, 07:22
2002-08-26, 07:45
2003-09-15, 07:10
2003-09-15, 05:28
2003-09-17, 03:19
2003-09-17, 03:50
2004-07-25, 08:25
2004-07-25, 08:51
2004-07-28, 06:43
2006-08-12, 07:04
2006-08-12, 06:33
2006-08-13, 06:41
2006-08-13, 05:50
2007-08-14, 06:05
2007-08-14, 06:33
2007-08-14, 09:09
2007-08-17, 05:52
2007-08-17, 06:18
2007-08-17, 07:15

Both H and K-band images are dominated by patches of bright cloud standing out against an otherwise dark atmosphere. Unlike similar observations of Uranus, the K-band images of Neptune show nearly as much detail as the H-band images,

indicative of the much higher cloud tops on Neptune (see Fig. 1). In 2001 and 2002, the clouds had a maximum coverage and brightness, essentially forming two zonal bands, the southern one centered at $\sim 40^\circ\text{S}$ and a northern extending from the limb down to $\sim 20^\circ\text{N}$. In subsequent years, the bands become fainter and more broken. Discrete features at other latitudes were also noted, as well as cloud visible in the H-band images, suggesting clouds at a range of heights.

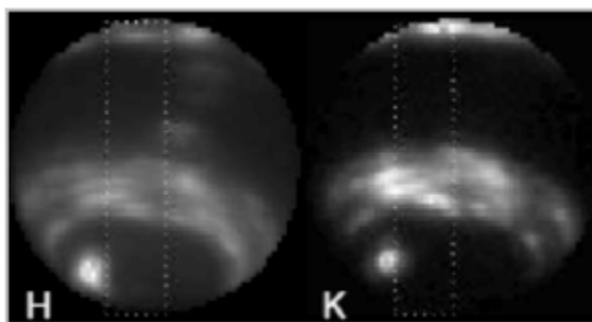


Figure 1. H-band and K-band images of Neptune from September 4, 2001 showing prominent bright, clouds in both filters. The contrast in the K-band is indicative of the clouds great heights.

Spectra show the bright bands and discrete features as visible at nearly all wavelengths, with exception of the peak methane absorption lines. In the deepest sensing wavelengths of the H-band, there is enhanced reflectance across all latitudes, suggesting a relatively uniform deep cloud (See Fig. 2.)

At a resolution of 40 mas per pixel, Neptune covered ~ 59 pixels in diameter in the 1024 X 1024 array images, with corrected seeing discs estimated to be about four to seven pixels in diameter near the planet center based on the full-width of satellites. This corresponded to a resolution of roughly 3330 km to 5825 km at the sub-observer point on Neptune, depending on the seeing and AO performance, and was far short of being diffraction limited. No attempt was made to deconvolve the images with the

presumed atmospheric point spread function in order to mitigate the affect of imperfect atmospheric seeing. See the discussion in the previous chapter on Uranus for a discussion on the risks and benefits of image deconvolutions.

The data were reduced and photometrically calibrated using standard techniques for near-infrared spectra and images, including flat-fielding, sky-subtraction, and interpolation to remove bad pixels. The faint standard star, FS34 was used for flux calibration, while a number of solar-type stars (SAO 163989, SAO 164580, SAO164338, SAO 146135, SAO 163616) were used as solar proxies, allowing us to express the calibrated spectra into dimensionless units of I/F.

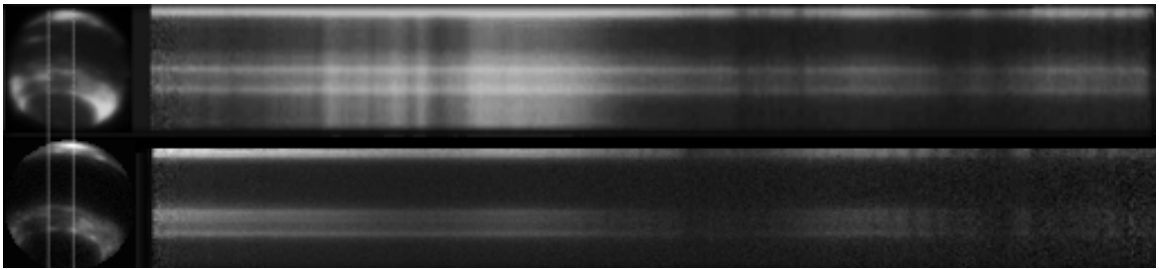


Figure 2. (Top) H-band image and spectra from September 2, 2001. The brightest clouds are visible across nearly all wavelengths, indicative of their substantial height. In contrast, the greater reflectance across all latitudes towards the center of the spectra suggests a relatively uniform cloud at depths only visible in the deeply penetrating wavelengths. (Bottom) Corresponding K-band image and spectra. Only the highest clouds are visible.

Passing through a 0.5 arc second slit (~ 13 pixel), the observed flux was dispersed by grating prism across the 1024-pixel detector at a resolution 0.285 and 0.332 nm/pixel for H and K, respectively, with resolving powers of roughly $R \sim 1500$. The final calibrated spectra were binned by a factor of 13 to match the spectral resolution set by the spectrographs projected slit width, for an effective spectral resolution $R \sim 115$.

Spectra were calibrated in wavelength by comparison with known spectral lines of planetary nebula NGC 7027 and carefully corrected to remove errors due to imperfect sky subtraction and occasionally detectable tilts of the slit relative to the detector.

3. Analysis

3.1 Spectral transmissions and parameter sensitivities

Aerosol scattering and wavelength-dependent molecular absorption of sunlight shape the spectra of Neptune in the H and K bands. The observed spectra can be modeled as light scattered by aerosols and attenuated by methane and collisional-induced absorption (CIA) by hydrogen. Figure 3 shows the atmospheric pressure heights corresponding to a single optical depth of attenuation along the two-way path for reflected sunlight at normal incidence. The calculations assume a stratospheric methane mole fraction of 1.6×10^{-4} and a deep methane abundance of 4% for pressure greater than 2 bars, consistent with modeling results.

The approach to constraining the aerosols and methane abundance follows the same reasoning applied to Uranus in the previous chapter. The hydrogen abundance and resulting absorption are assumed to be reliably known, and thus can be used to constrain the aerosol reflectance at heights and wavelengths dominated by hydrogen CIA. With the aerosol reflectance determined at a given pressure, the methane abundance may then be inferred from the reflectance in methane bands sensitive to the same pressure levels. Differences in the methane profiles (and to a much lesser extent, local gravity and temperature) lead to differences in the transmissions and sensitivities

between Uranus and Neptune. Figure 3 shows that hydrogen absorption dominating in the K-band provides constraints on aerosol scattering between ~300 mbar and ~50 mbar. Though within this range, methane also begins to affect reflectance between ~90 mbar and ~50 mbar, so the potential for slight correlations between the aerosol and methane abundances at these heights should be considered.

Given the observed enhancement of methane in the lower stratosphere, the methane opacity in the strongest absorption features becomes significant at lower pressures than expected for Uranus—low enough to sample the heights at which aerosols are constrained. This suggests that the methane could be retrieved in the ~300 to ~120 mbar range in the H-band, as well as the ~90 to ~50 mbar range in the K-band, with little degeneracy between parameter solutions. Above and below these heights, the solutions are ambiguous. Either the methane or the aerosol scattering may be retrieved, but not both. As with the analysis of Uranus, the methane abundances were restricted in values based on modeling assumptions discussed in the Section 3.3.

3.2. Atmospheric Model

The model was qualitatively identical to that used for the modeling of Uranus. Seventy layers of gas and aerosols, with methane coefficients as prescribed by Sromovsky et al., (2011) and hydrogen CIA opacities were computed using coefficients of Borysow (1996), adapted for arbitrary para-hydrogen fractions by Daphne Stam (private communication). The para-hydrogen fraction was initially a free parameter to test for possible disequilibrium; however, subsequent testing demonstrated that error in this retrievals was up to 30%, and this far exceeds the expected ~10% or less magnitude of disequilibrium inferred from Voyager IRIS

measurements (Conrath et al., 1989; Fletcher et al., 2014). As such, the hydrogen para-fraction was thus set to the local thermodynamic equilibrium fraction. A temperature profile from Lindal et al. (1990) was used at all latitudes, while local gravity was treated as function of latitude but constant in height.

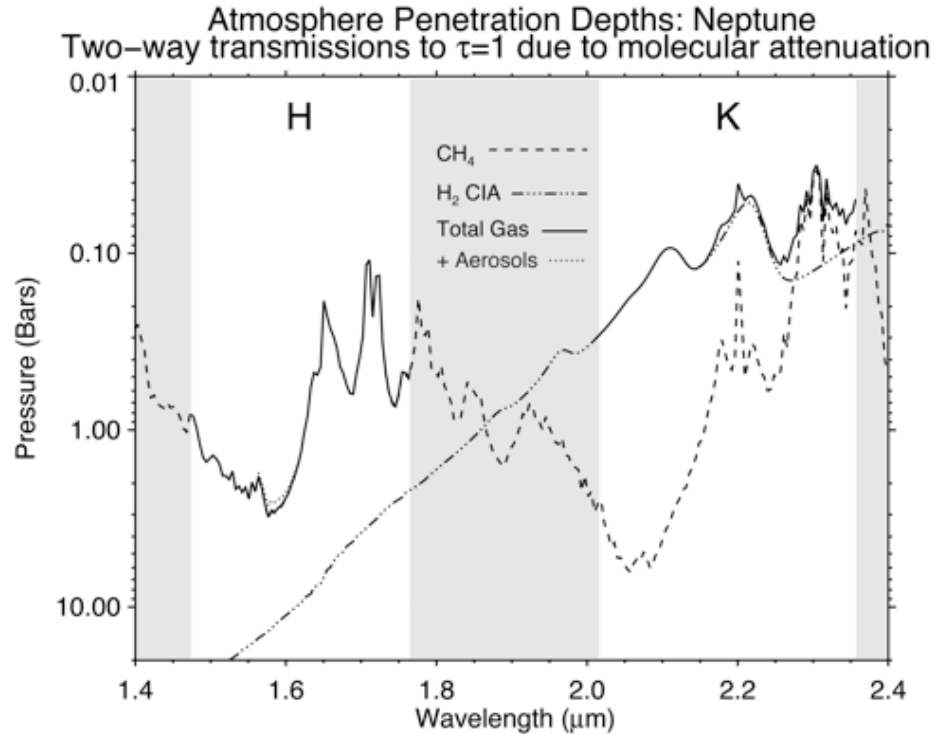


Figure 3. Atmospheric pressure heights corresponding to a single optical depth of attenuation along the two-way path for reflected sunlight at normal incidence. Different components to the attenuation are plotted separately. Weak methane absorption dominates in the H-band; collisional induced absorption by hydrogen dominates the K-band. Wavelengths beyond the filter ranges are shaded in gray. Aerosols only become significant in the deepest sensing regions of the H-band. The calculations assume a stratospheric methane mole fraction of 1.6×10^{-4} and a deep methane abundance of 4% for pressure greater than 2 bars, and the mean retrieved aerosol distribution as reported in Section 4.

Values of the methane mole fraction and aerosol scattering optical depth per bar of pressure were specified for each layer. Cumulatively, the layers define vertical

profiles for the methane and aerosols. These profiles were partly free parameters, though partly restricted due to the limited information content of the data, as discussed below. Ultimately, the profiles were optimized to produce modeled spectra most consistent with the observed spectra.

3.2.1. Modeled Methane Profile.

Constraints were placed on the vertical distribution of methane. This was necessary given the limited information content of the data and the degeneracy between methane and aerosol profiles and most pressures. The data can potentially constrain the methane mole fraction around the tropopause if the abundance of aerosols and methane are great enough to produce an adequate spectral signature. Below these heights, the distribution of either methane or aerosols must be assumed in order to retrieve some dependent distribution of the other. Since the aerosols distribution may reflect multiple condensed species (potentially including H₂S, and photochemical products as well as CH₄) and clearly displays spatial variability, whereas the methane profile may plausibly follow a roughly temperature-limited saturation curve, the choice was made to fix the methane abundance at most heights.

The assumed methane mole fraction below several hundred millibars was based on proposed mixing ratio profiles of Karkoschka and Tomasko (2011). Karkoschka and Tomasko (2011) had greater sensitivity to the deep methane abundance due to HST-STIS observations between 820 nm and 832 nm; at these wavelengths hydrogen CIA dominates, allowing for constraints on the aerosol reflectance and subsequent constraints on the deep methane abundance. Applying

their results to present analysis, two cases were tested—one with latitudinal variation in the methane profile, as favored by the HST-STIS analysis, and the second with no latitudinal variation. As with Uranus, the resulting fits from each were compared to evaluate the goodness of the fits for each assumption. Profiles assuming a polar depletion of methane consistently provided better fits to the data. The polar depletion models were thus adopted for all results in this study to fix the methane mole fraction at pressure greater than 300 mbar.

At pressures less than 300 mbar, the data provides some constraints, but test show the precise distribution is still only marginally constrained. Weak correlations with the aerosol distribution and sensitivities in the initial conditions can still produce slight spurious structure. To mitigate these concerns, two additional constraints were applied: firstly, the methane profile was not allowed to exceed the saturation vapor pressure at any height, based on physical arguments; secondly, to produce more easily comparable results consistent with the information content of the data, the mole fraction was modeled as freely fit but uniform in height above 50 mbar.

3.2.2. Aerosols Scattering and Reflectance

Aerosols distributions were modeled following methods of Banfield et al. (1996, 1998) and Stam et al (2001), and identically to the methods applied to Uranus in the previous chapter. An effective aerosol scattering optical depth, τ_s , was defined as follows:

$$\tau_s(z, \lambda) = n(z) \sigma(z, \lambda) \varpi_0(z, \lambda) PF(\alpha, z)$$

Where n is the number density of aerosols per unit area, σ is the effective cross sectional area of each particle, ϖ_0 is the single scattering albedo of the aerosols, $PF(\alpha)$

is the normalized scattering phase function evaluated at the angle between light incidence and emission, and z and λ designate that parameters are a function of height and wavelength. In a single-scattering regime, the contribution to the observed reflectance from each layer is dependent on a product of all the above terms. The total reflectance due to single scattering can be found by vertically integrating over all layers down to sufficiently great atmospheric optical depths:

$$I(\lambda) = \frac{F(\lambda)}{4} \int_0^{\infty} n(z) \sigma(z, \lambda) \varpi_0(z, \lambda) PF(\alpha, z) e^{-\tau(z, \lambda)\mu_0} e^{-\tau(z, \lambda)\mu} \frac{dz}{\mu}$$

Where $I(\lambda)$ and $\pi F(\lambda)$ are the observed radiance and incident solar flux at wavelength λ , $\tau(z, \lambda)$ is the total atmospheric optical depth from the top of the atmosphere down to height z , and μ_0 and μ are the cosines of the incidence and emission angles, respectively.

The wavelength dependence to the scattering was modeled through adjustments of the scattering cross section. Physically, this assumes the particles have an effective shape and size for which the relevant wavelength-dependent extinction efficiencies can be computed using Mie theory.

3.3 Retrieval Algorithm

Constrained vertical profiles of aerosol scattering optical depth and methane mole fraction were simultaneously retrieved from both H and K spectra using an inversion algorithm. This follows Banfield et al (1996,1998) and Stam et al (2001) and is identical to that used for retrieval of Uranus in the previous chapter, where further details are provided. The method aimed to retrieve the simplest solutions possible while minimizing differences between observed and modeled spectra. The

profiles evolved iteratively, as new functional derivatives were computed each iteration to account for non-linearity in the solutions. Smoothness constraints and vertical correlation scales were applied to prevent insignificant changes in the spectrum from producing significant changes in the vertical profile. The values of these constraints were optimized based on test retrievals using synthetic data (described below) and the noise and information content of the real data.

3.3.1 Retrieval Uncertainties. Retrievals of known profiles from forward modeled spectra with realistic noise were performed to refine the constraints and estimate the uncertainty in retrieved parameters. The synthetic retrieved quantities were subtracted from the true profiles for 250 cases and percent error was computed (see Figure 4). These ensemble tests suggest that retrieved values of $\tau_s \text{ bar}^{-1}$ were typically less than 20% between the 150 mbar and 50 mbar heights, increasing to 50% between 200 mbar and 1 bar. Around 2 bars the error drops to roughly 20%. The methane mole fraction was typically accurate to within 30%, above 100 mbar, though errors can seldom be as large as 40% in low albedo regions where the signal to noise ratio is lower. Further testing indicates that the retrievals tended to systematically underestimate the methane mole fraction in the lowest albedo regions by roughly 35%. In such cases, the goodness of the fit has a broad minimum over a ~40% range of methane values. The systematic nature can be explained by the tendency of the profile to remain near the more moderate initial conditions when small changes produce little improvement.

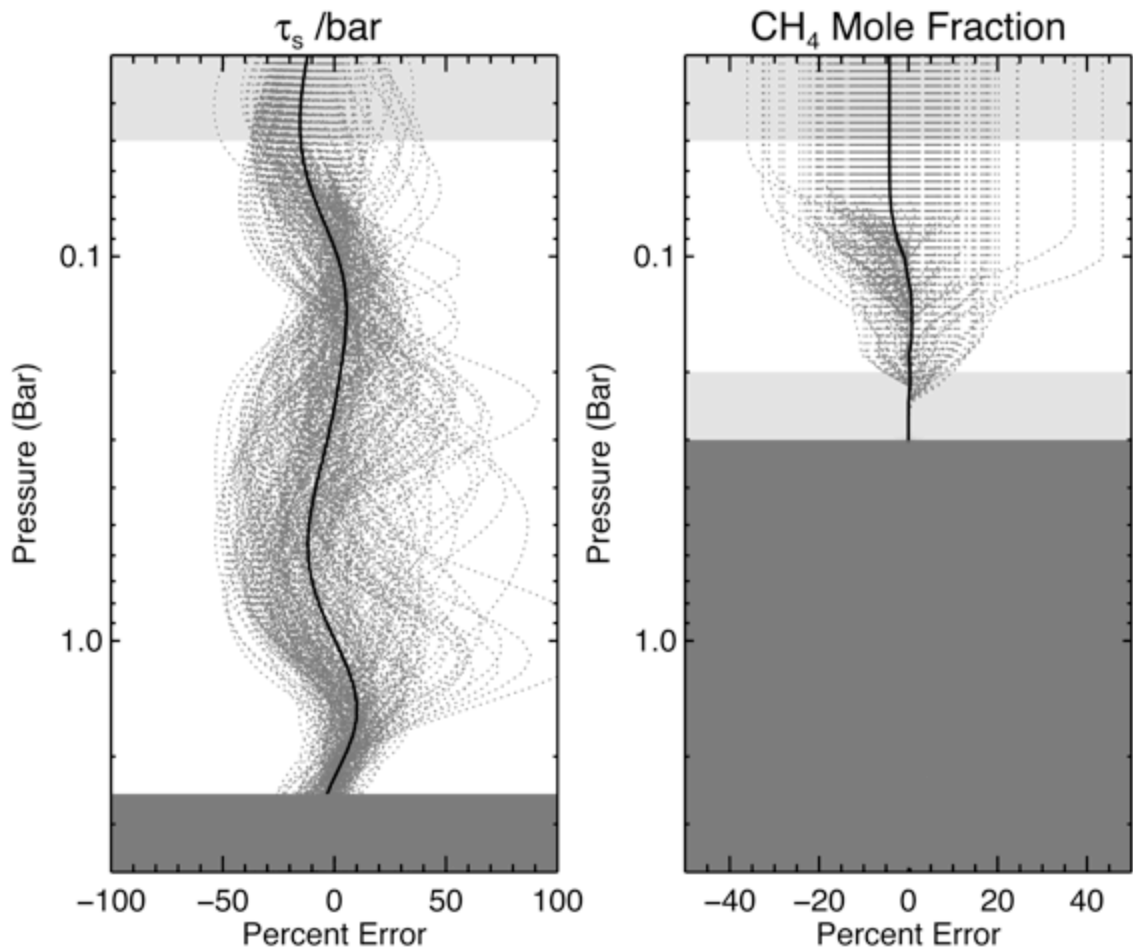


Figure 4. The difference between retrieved solutions to the vertical profiles and the true profiles that produced the synthetic spectra, as a percentage of the true profiles. The plots show the result of 250 retrievals, with the mean value in black. The shaded regions show where the data content diminishes and results are strongly dependent on the initial conditions and assumed profiles. The darkly shaded regions (in the methane profile) indicate fixed parameters.

Systematic uncertainties in the calibration may affect the results. Blurring due to the atmosphere can reduce the intensity of the smallest, brightest features. The effect can be estimated from the deconvolutions applied to test cases of Uranus in the previous chapter. Uncertainties in reflectance towards the edges of the disk and along

boundaries of high-contrast features may be as great as 30%. For single scattering, this should lead to roughly comparable errors. Many of the features on Neptune cover an area larger than the typically observed point spread function (roughly 4 pixels FWHM), and so the errors are expected to be far less than 30% for most cases.

Finally, since single scattering is assumed, errors may result in instances where the aerosol optical depths exceed a tenth. For $0.1 < \tau < 0.3$, double scattering likely occurs and for $\tau > 0.3$, higher orders of scattering are likely. This has the effect of reducing the total scattering optical depth necessary to produce an equivalent reflectance, as discussed in the previous chapter on Uranus. Assumptions regarding the scattering phase function and single scattering albedos affect this result. For the highest optical depths encountered in the retrievals, scattering optical depths may be overestimated by as much as 45%; for a majority of the data, the error is less than 10%. Quantitative conclusion derived from these results should consider this caveat.

4. Results

Scattering optical depths and methane mole fractions were retrieved as a function of pressure and latitude for each of the 27 observations in the data set. Scattering optical depths were expressed as $\tau_s \text{ bar}^{-1}$ at $1.48 \mu\text{m}$. Profiles of methane mole fraction were constrained by both observations and a priori assumptions, with the data determining the mole fraction at roughly 60 mbar.

4.1 Retrieved aerosol scattering optical depths

The vertical profiles of aerosols consistently displayed two distinct layers: a variable optically thin haze at or above the tropopause and a deeper relatively uniform layer. The top layer represents the prominent bright clouds seen in the H and K-band

images. It has an average height of $\sim 100 \pm 15$ mbar though clouds do appear higher in the northern hemisphere than the southern hemisphere, as noted in previous observation by several authors (Gibbard et al., 2001, Roe et al., 2001). Clouds at the northern edge of the observations are as high as 45 ± 15 mbar in contrast to the highest southern hemisphere pressures of 90 ± 15 mbar (see Figure 5).

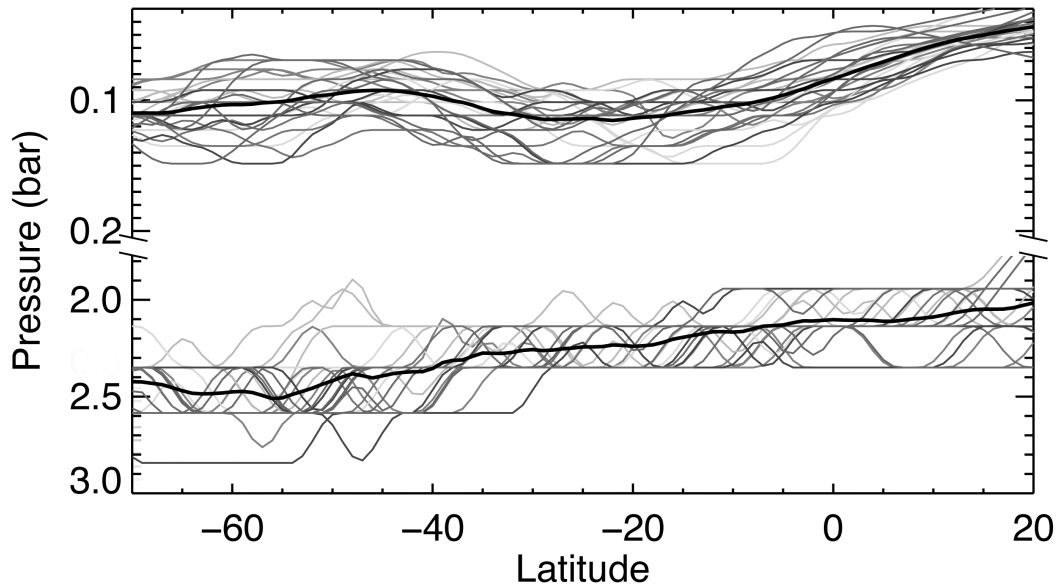


Figure 5. The peaks in aerosols scattering optical depths for the two main layers versus latitude. The dark solid line represents the mean values. The plot shows a trend in the retrieved cloud heights in both layers, decreasing in pressure towards the northern hemisphere.

The retrievals show this top layer as fairly continuous but highly variable in optical thickness. The scattering optical depth per bar of pressure for this cloud can vary by up two orders of magnitude between latitudes. Disk averaged values of the aerosol profiles are shown in Figure 6, while Figure 7 shows plots of the scattering profiles for 45°S and 1°N , color-coded by year. Uncertainties are roughly 20% at the cloud peaks as discussed in Section 3.3.1. The highest values observed were in 2002, when the brightest features had a $\tau_s \text{ bar}^{-1}$ of ~ 8 ; integrated over the layer, this adds up

to a total scattering optical thickness of ~ 0.43 . The same image at 1°N latitude had a τ_s bar^{-1} of ~ 0.28 , or an integrated τ_s of only ~ 0.02 . Similarly low scattering optical depths can be found at 40°S in other years.

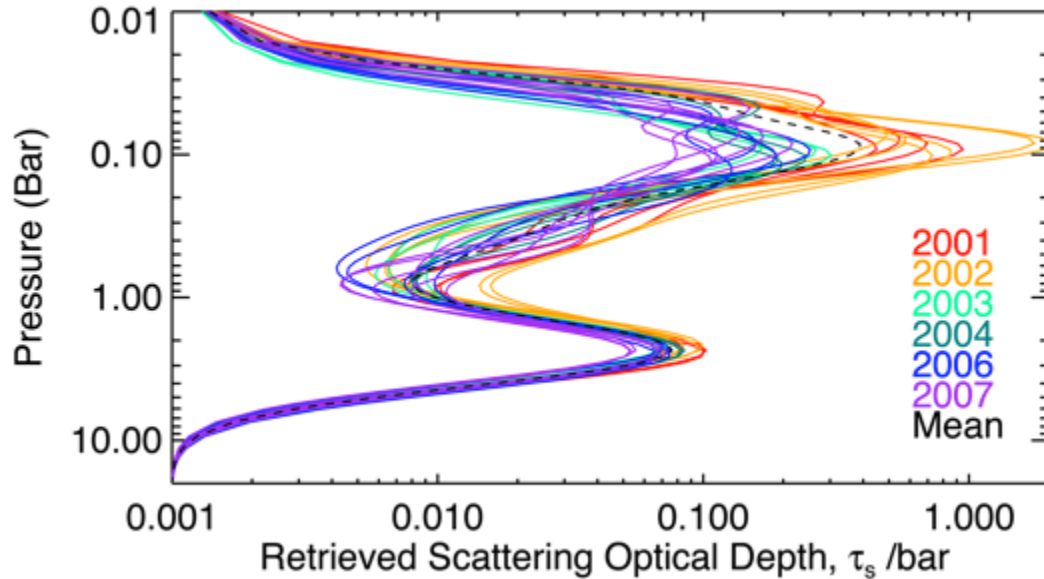


Figure 6. Disk averaged profiles of retrieved aerosol scattering per bar versus pressure. The observations are color coded to indicate the year. The mean value is the black dashed line.

The deeper layer of aerosols showed considerably less variability, reducing by 50% in disk-averaged values over the observed period. Latitudinal variation could be as large as a factor of three, with the highest values found at roughly the same latitudes as the brightest high clouds. This correlation does not appear to be artificial, as the two layers are separated by 3-4 pressure scale heights, and thus contribute reflectance to largely different portions of the spectra. The deeper cloud layer peaked at a mean pressure of ~ 2.3 bars with a mean τ_s bar^{-1} of ~ 0.078 and roughly 20% uncertainty. The vertically integrated tau of this deepest layer varied between ~ 0.10 and ~ 0.28 .

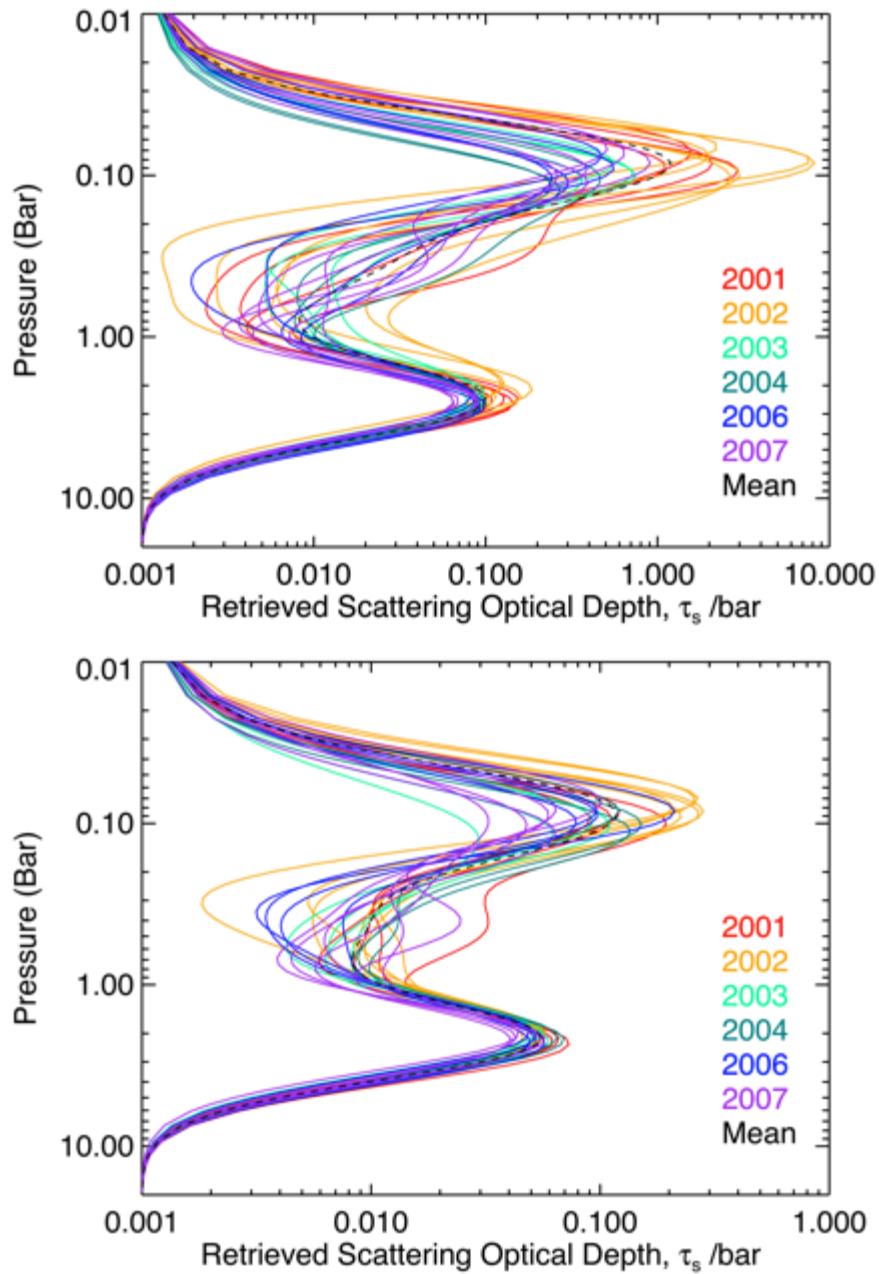


Figure 7. Plots of the scattering aerosol optical depth per bar versus pressure. (Top) Retrievals for each observation at 40°S latitude. (Bottom) For observations at 1°N latitude. Note the difference in abscissa values. Values at the peaks have an uncertainty of 20% and up to 50% elsewhere. Plots are color coded to indicate the year. The mean is shown in black (dashed).

Contour plots of aerosol scattering profiles clearly illustrate the variation in height and latitude. Figure 8 shows one example from 2002. In these plots, the bright clouds can be seen as patches of enhanced aerosols above 100 mbar at 40°S. The bright patch north of 20°N is clearly at a lower pressure. The cloud at roughly two bars is also seen to be enhanced between ~70°S and 30°S relative to other latitudes, roughly aligning the top layer. Pressures between the two cloud layers have larger uncertainties—up to 50%—and much of the fine structure there may be spurious. The region of enhanced aerosol scattering extending below the high bright feature just north and south of 40°S adds to banded reflectance seen in the accompanying image. The clearing in the northern hemisphere is likely real, but potentially exaggerated. Similar plots for all observations are shown in Figure 9.

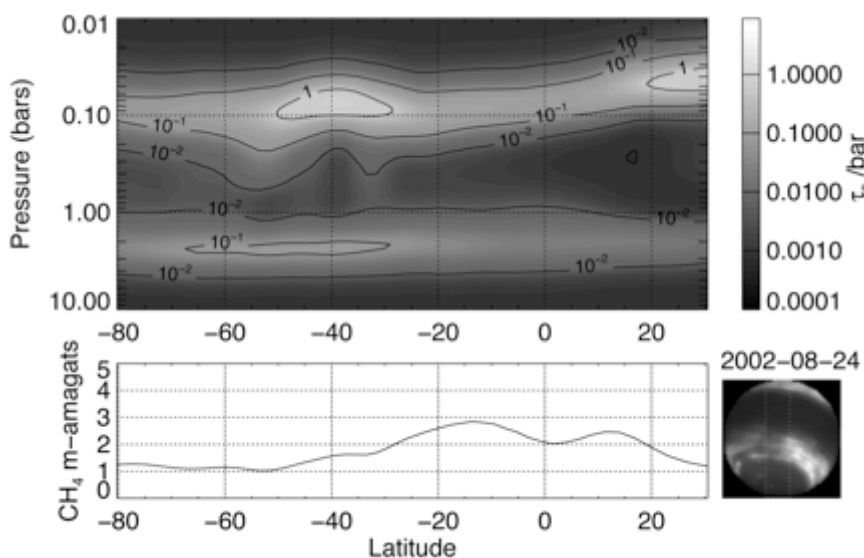


Figure 8. (Top) Retrieval showing the retrieved aerosol scattering optical thickness per bar of pressure as a pressure and latitude for an August 24, 2002 observation. Note that the top layer is continuous in latitude, but varies in density and height. (Bottom) A plot of the m-amagats of methane retrieved above the 100 mbar level versus latitude.

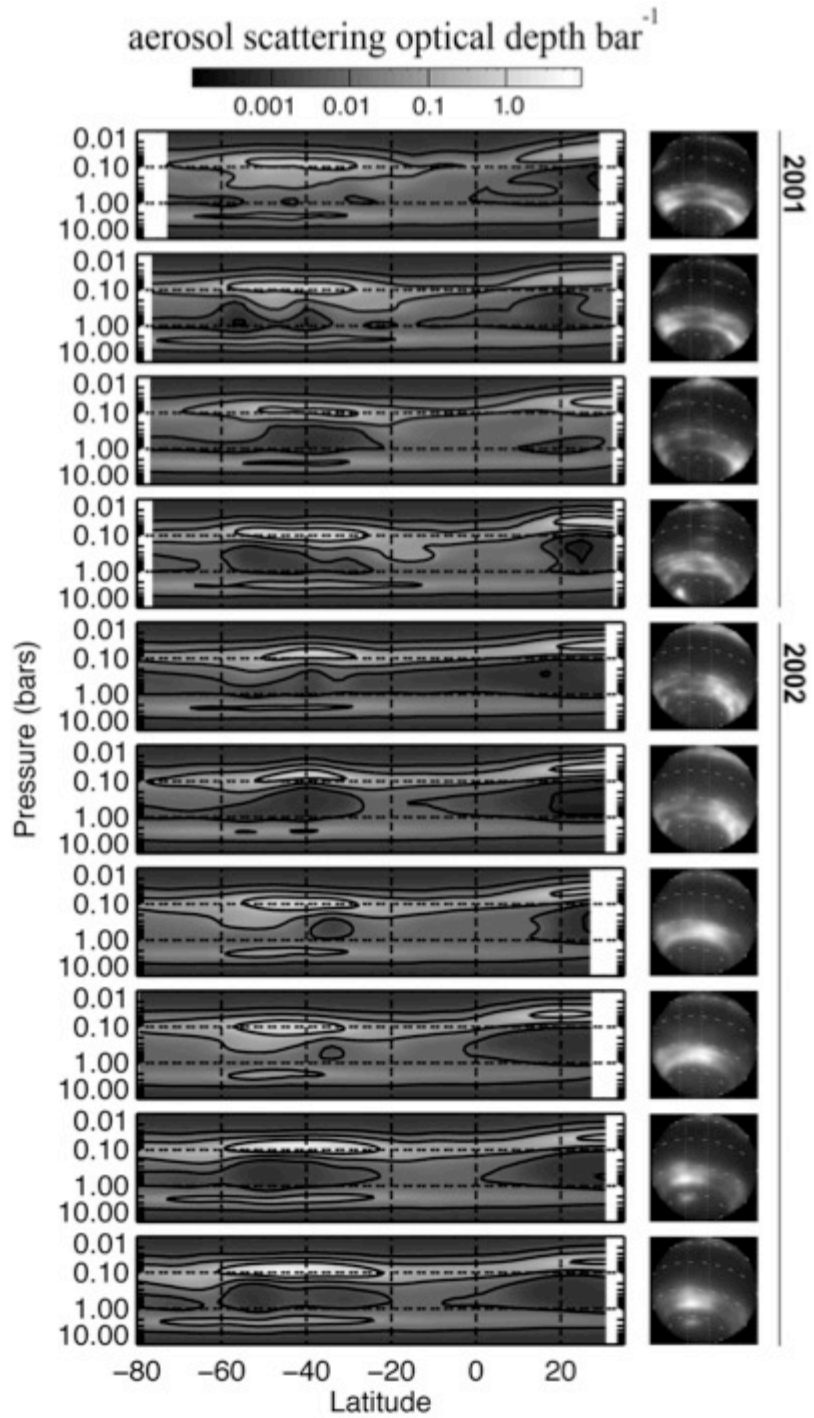


Figure 9. Retrieved aerosol scattering optical depths per bar as a function of pressure and latitude for each observation. Contours mark 1.00, 0.10, and 0.01 $\tau \text{ bar}^{-1}$. Corresponding H-band images are shown at the right, with the dotted contours marking 30° intervals in latitude and the projection of the spectrograph slit. The year of the observations are indicated at the right.

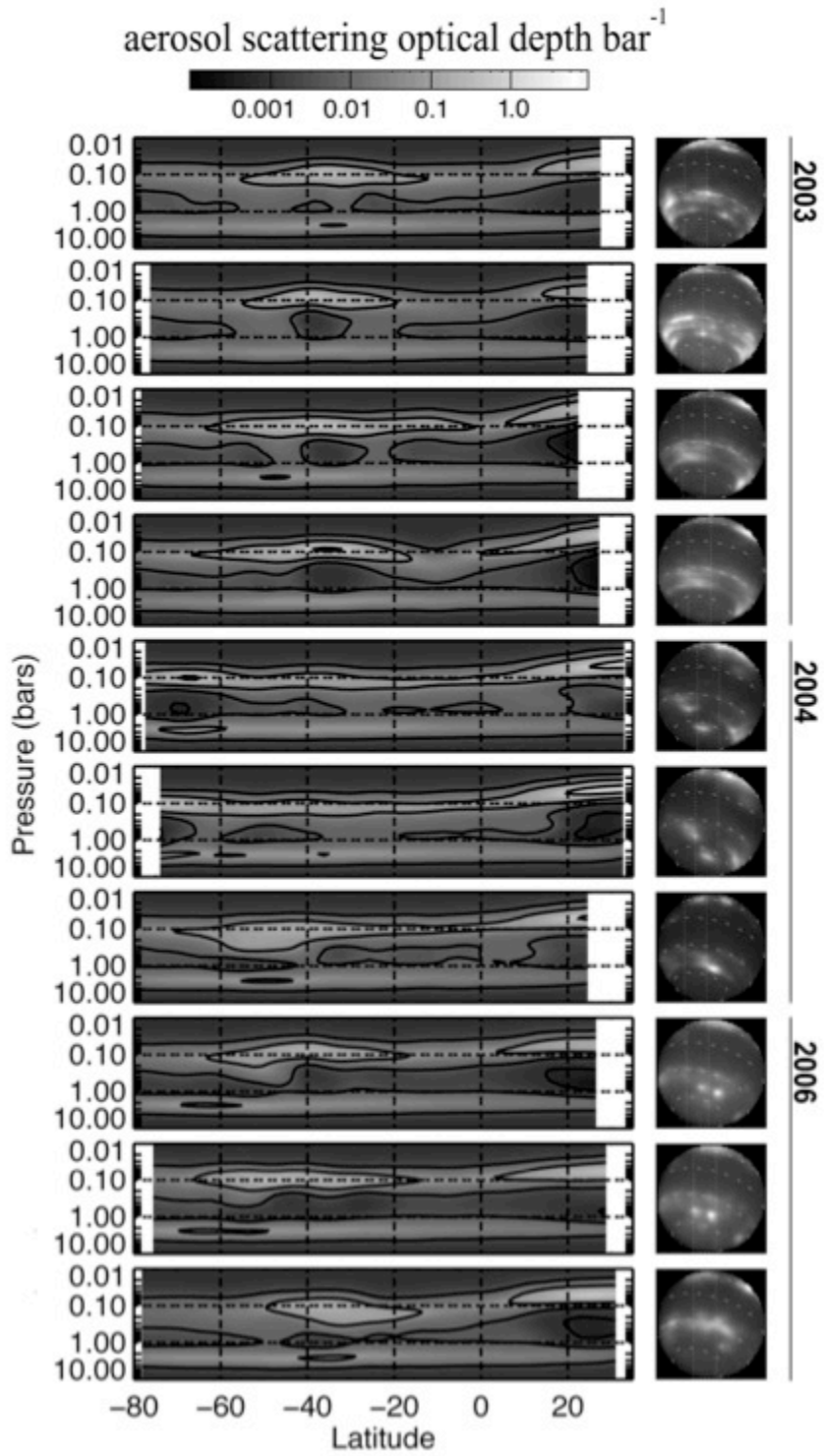


Figure 9. Continued

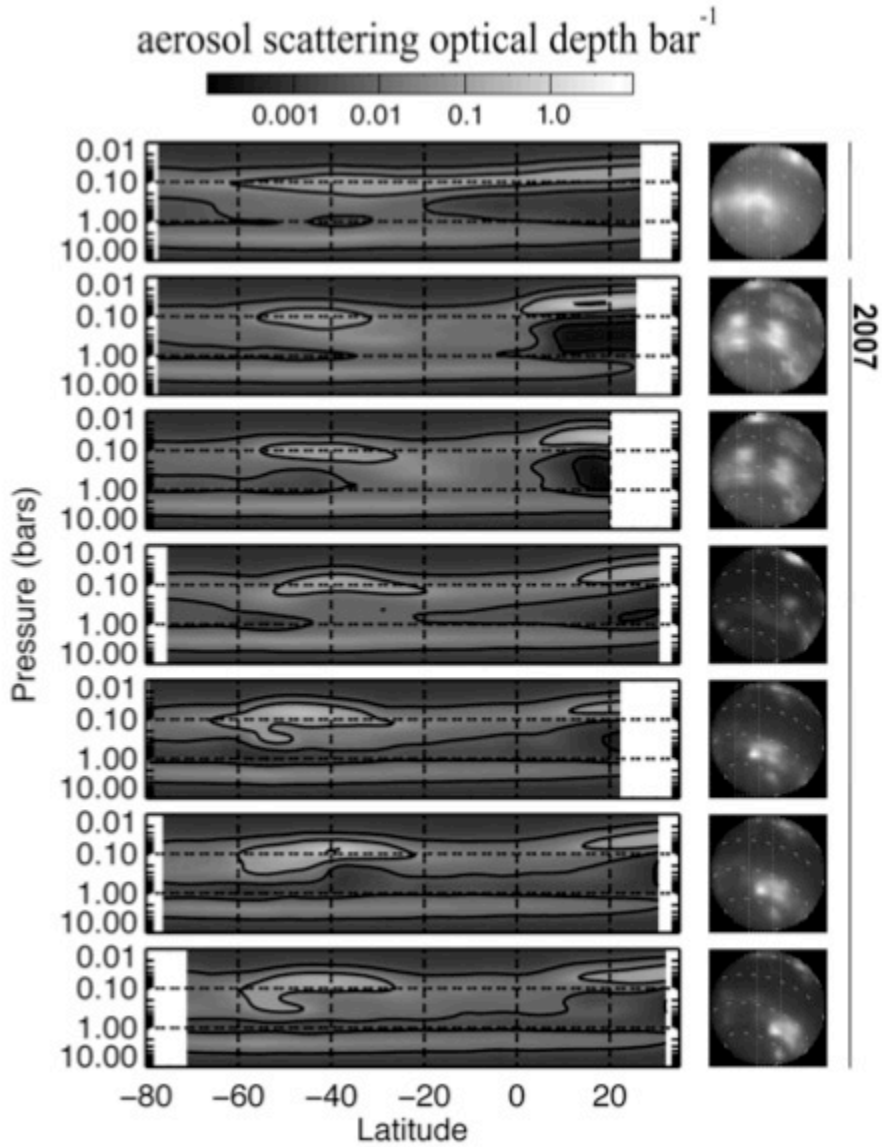


Figure 9. Continued.

Finally, the vertically integrated aerosol scattering optical depth displays the total change in aerosols as function of time and latitude as shown in Figure 10. Most of the aerosols are concentrated around 40°S latitude, particularly in 2001 and 2002. Total scattering optical depths are still less than unity. In the completely conservative scattering case, this would imply that the gas limits transmission even in the brightest

regions; however, since the scattering optical as defined here is a product of terms, the clouds effective extinction could be larger if any of the component terms reduce the reflectance (e.g. the number density could be higher if the be particle single scattering albedos were very low). These data cannot place constraints upon the single scattering albedos or scattering phase functions and hence interpretations will have to rely upon assumptions and the findings of others. The wavelength dependence of the highest aerosol scattering, however, can be roughly constrained by the present observations since the brightest high clouds contribute reflectance over the entire observed spectrum. Best fits were found to correspond to particles with effective mean radii of 0.6 to 0.8 μm . Particles could be slightly larger ($\sim 1 \mu\text{m}$), but no smaller than $\sim 0.5 \mu\text{m}$ without significantly worsening the fits.

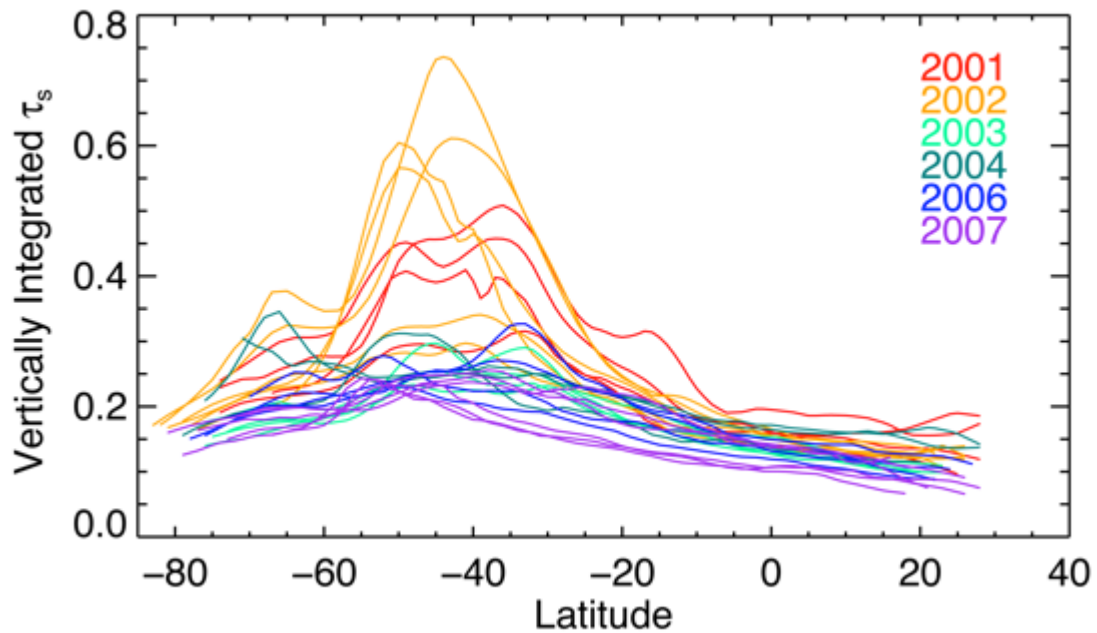


Figure 10. Vertically integrated aerosol scattering optical depths versus latitude. Values were integrated from 1mbar down to the base of the bottom layer cloud.

All the aerosol scattering figures show a drop in the scattering from 2002 to 2003. The highest values drop by more than an order of magnitude and continue so for the remainder of the observed period. This evidently marks a transition in cloud activity. Observations from Karkoschka (2011) ranging from 1994 to 2010 showed that this active period began in 1998. The relatively cloudless period continued to at least 2010.

4.2 Retrieved methane mole fraction

The methane mole fraction in the lower stratosphere was inferred from retrievals of constrained vertical profiles. The disk and annually averaged results are shown in Figure 11. The mean value at 60 mbar was 1.3×10^{-4} with an uncertainty of 30% given the constrained structure. If the profile is unconstrained above 300 mbar and permitted to exceed saturation, the mole fraction was found to range between 9×10^{-5} and 4×10^{-4} . These values are lower than that determined from observed center-to-limb behavior in 727 nm and 890 nm methane bands, which yields a mixing ratio less than 1.7×10^{-3} with a nominal value of 3.5×10^{-4} (Baines and Hammel, 1994). It is also lower than the middle stratospheric value of $(1.5 \pm 0.2) \times 10^{-3}$ determined from Herschel-PACS observations (Lellouch et al., 2010). Such high values appear inconsistent with the present data and modeling techniques. Values as high as 3.5×10^{-4} may be tolerated with a doubling in the reduced χ^2 , but the fits are not preferred. The discrepancy may be attributed to differences in the modeling assumptions or observations. Neptune's disk in the Herschel-PACS data is from 2009, which is two years later than any data analyzed here. More intriguingly, the Herschel-PACS data is unresolved, and the resulting values reflect disk averages with greater contributions

from polar regions. If polar regions were enhanced in methane at stratospheric levels, this would be consistent with observations of polar hotspots that could raise the local methane saturation vapor pressure and allow for seepage into the stratosphere (Orton, et al, 2007).

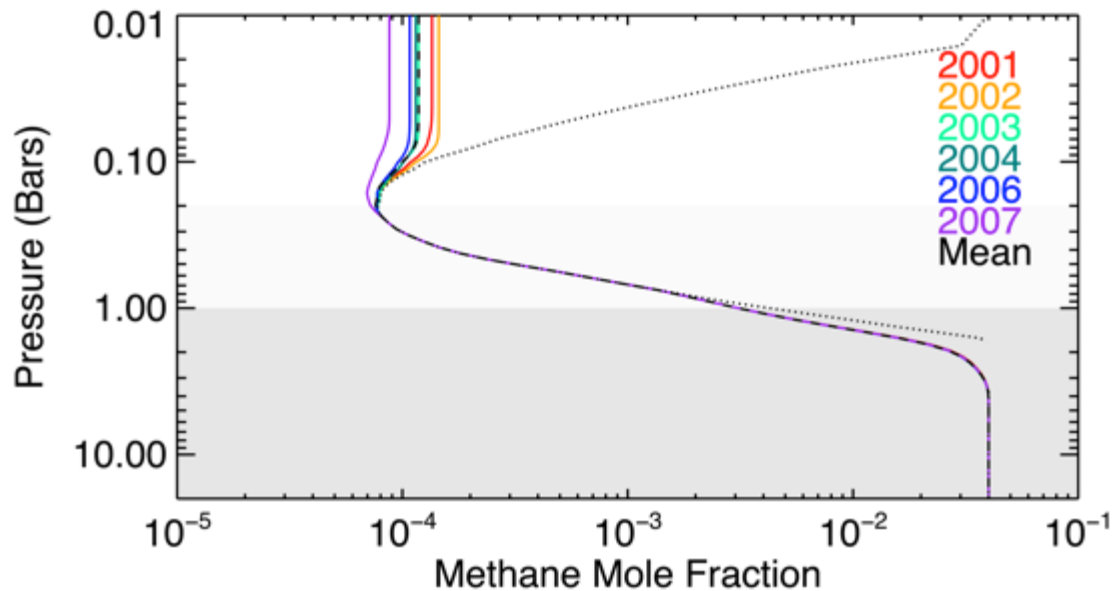


Figure 11. Retrieved methane mole fraction as a function of pressure for constrained profiles, averaged and color-coded for each year. The mean is shown as the black dashed line. The equilibrium saturation vapor pressure is shown as the dotted line. The area shaded in dark gray is held constant during the retrievals, and adjusted only as a function of latitude. The lightly shaded region transitions between the fixed portions of the profile and the more freely fitted portion. The profile is still constrained to remain below saturation and become uniform at the top.

The 60-mbar methane mole fraction and m-amagats of methane above the 100-mbar level are plotted in Figures 12 and 13. These values are similarly somewhat low when compared to other published values. Karkoschka and Tomasko found that methane abundance above the cloud tops, as inferred from 2003 HST-STIS spectrograph data, was 2.6 and 1.7 m-amagats for the southern and northern

hemisphere, respectively. As Figure 13 shows, at least one observation from 2003 approaches these published values, but the mean is closer to 1 m-amagat.

The variations in latitude exhibited in the plots 12 and 13 are intriguing if they can be believed. It appears the highest values are fairly well correlated with the highest values of $\tau_s \text{ bar}^{-1}$ for the upper cloud. Synthetic test demonstrate that latitudinal variation of this magnitude should be retrievable. Although the retrieved values in low albedo regions can be systematically darker by 40%, the differences seen here generally exceed that amount. Nonetheless, given the apparent discrepancy in the retrieved methane abundances and other published values, this pattern of latitudinal variation is in need of future verification.

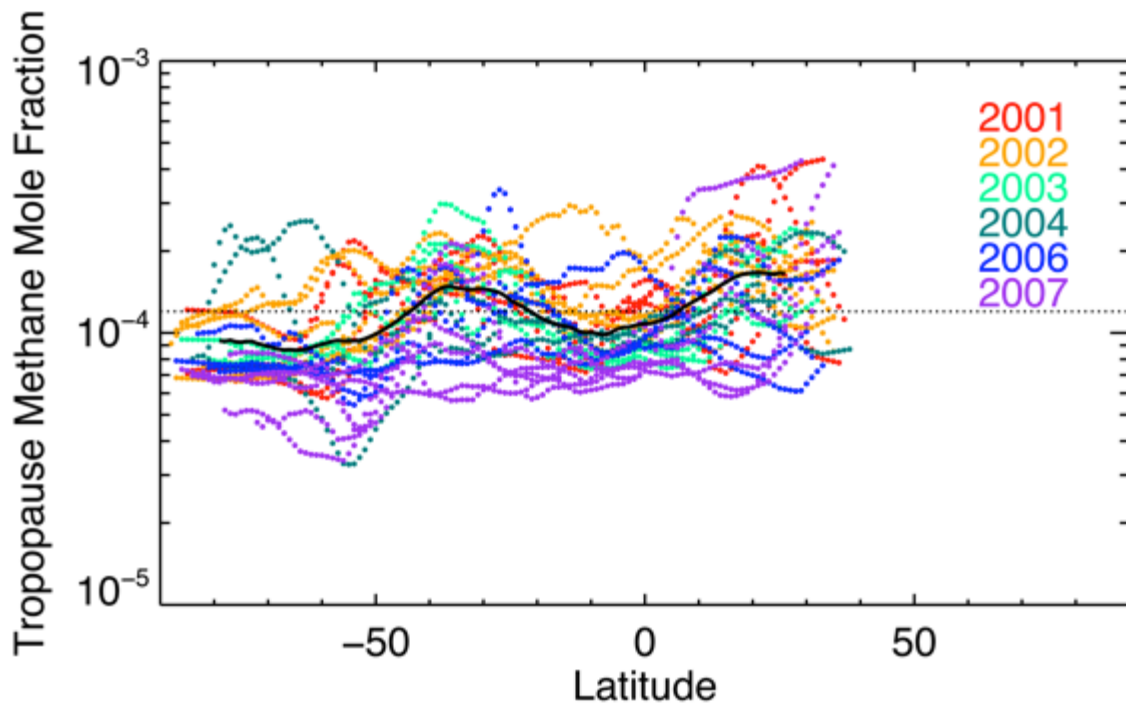


Figure 12. Methane mole fraction at the 60-mbar level versus latitude for each observation, colored to indicate the year. The black solid line represents the mean.

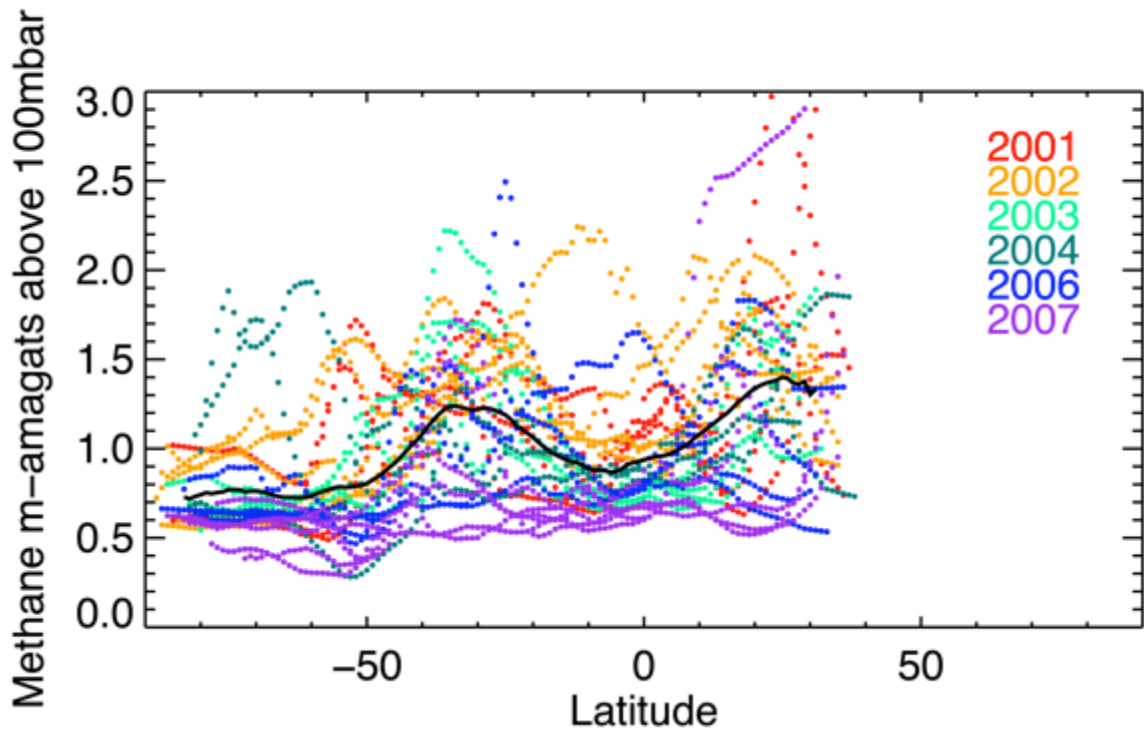


Figure 13. Similar to Fig. 12, but with M-amagats of methane above the 100-mbar level.

4. Discussion

With a consistent pattern of enhanced aerosol scattering optical depths, elevated cloud heights, and perhaps marginally greater methane abundance at mid-latitudes, the retrieved distributions are consistent with a pattern of general circulation that favors upwelling at mid latitudes and downwelling at the equator and polar latitudes. Such a model was proposed by Conrath et al. (1991, 1998) following an analysis of Voyager II IRIS data, and again by dePater et al. (2014) who synthesized observations ranging from microwave to near IR. Temperature fields show a minimum at $\sim 45^{\circ}\text{S}$ indicative of adiabatic cooling associated with rising plumes.

Likewise, measurements show a positive disequilibrium in the hydrogen para-fraction at these same latitudes, as would be expected if gas was raised from warmer depths (Conrath et al., 1998; Fletcher et al., 2014).

As noted, the clouds that mark these latitudes of upwelling may be associated with vigorous updrafts, vortices, or a combination of the two. dePater et al. (2014) argues that plumes may generate anticyclones as rising plumes decelerate and spin up anti-cyclonic vorticity upon reaching the stable heights of the stratosphere. Air forced to rise over these circulations can be cooled to saturation forming clouds similar to the companion clouds seen in Voyager images. Continued upwelling at mid-latitudes would presumably lead to enhanced methane mixing ratios and colder temperatures relative to other latitudes, allowing clouds to persist. If fallout times are long enough, it is conceivable that wind shear may spread these vortex-produced clouds over many longitudes producing the zonal banding observed in 2001 and 2002.

As used to discuss the Uranus cloud feature in the previous chapter, a parcel theory analysis was applied. This approach provided rough estimates of expected lifting heights and aerosol mass for different scenarios in order to evaluate the consistency between observations and theory. The retrieved aerosol scattering optical thickness at 40°S relative to lower albedo latitudes is shown in Figure 14. This amounts to a total scattering optical depth enhancement of 0.086 τ at 84 mbar. Assuming aerosols with a single scattering albedo, $\omega_0 \sim 0.99$, a density of $\rho \sim 0.5 \text{ g cm}^3$, an effective mean radius of $\sim 0.7 \text{ } \mu\text{m}$ (as consistent with the best fits), a normalized scattering phase function evaluated at scattering angles of $\sim 179^\circ$ to be ~ 0.6 , and an extinction efficiency of ~ 2.0 , the retrieved mean optical thickness

enhancement of the high clouds at 40°S equates to roughly 0.017 g per unit area of condensate. Assuming the same Lindal et al. (1990) temperature profile and the average retrieved methane profile for mid-latitudes (~57% relative humidity at the starting height), ~0.017 g m² mass can be condensed by lifting a parcel from 92 mbar to 74 mbar. This would require ~5 J/kg of energy, equivalent to a ~3 m/sec updraft, if the parcel were rising vertically across the density gradient of a stable layer. This would correspond to a temperature drop of ~4 K over a rise of 20% of a scale height, or about 3 km. Less lift is needed if the methane abundance is greater. If assumed saturated (i.e. 100% relative humidity) at its starting pressure, then the parcel may begin at 84 mbar and rise to 79 mbar, with only 0.2 J/kg, or 0.6 m/sec updraft required, resulting in a 1.4 K temperature drop over 1 km, or ~6% of a scale height. In their EPIC modeling, Stratman et al, (2001) found that modeled clouds best matched Neptune's companion clouds in appearance when created by a 3 mbar and 1 K drop, from 76 mbar to 73 mbar, or about 0.5 km and 4% of a scale height. Considering the differences in modeling approach, these results are quite comparable. There is room for adjusting all the values, but the general conclusion is that the upper troposphere and lower stratosphere have enough methane to produce clouds consistent with the majority of retrieved scattering optical depths. The greatest optical depths retrieved in 2001 and 2002 require lift to lower pressures (~70 mbar) and smaller particle sizes (~0.5 μm), which would still be consistent with the data, or about 45% supersaturation—a factor of three greater than the retrieved results—or some combination of the above.

Can such a cloud extend across longitudes to produce the zonal appearances seen in the data? If aerosols move with the parcel that rises over a vortex and then descends back to its original height, the aerosol may be expected to evaporate upon descent and preclude an extended cloud; however, if the atmosphere becomes saturated due to strong upwelling at given longitudes and latitudes, clouds triggered by ascent may persist. A rough estimate of the aerosol fallout rates in the lower stratospheric heights may be given by the Stokes terminal velocity, defined as,

$$V = \frac{2g(\rho_p - \rho_{atm})r^2}{9\eta}$$

Where g is the local gravity, ρ_p is the particle density, ρ_{atm} is the atmospheric density, r is the particle radius, and η is the dynamic viscosity of the gas taken to be $\sim 3 \times 10^{-5}$ (Weast et al., 1987). This equals about 16 m/day for 0.7 μm radius particles, and half as fast for 0.5 μm particles. If the inferred 1 Km lift above the condensation level defines the thickness of the cloud, then particles may fall for ~ 120 days before falling below the cloud. Given wind speeds of $\sim 45 \text{ m s}^{-1}$ relative to the vortex (Stratman et al., 2001) the particles may be carried around the planet in roughly 30 days.

Neptune's change in appearance from 2002 to 2003 may be a result of changes in the methane mixing ratio at the tropopause. With less methane, the same amount of lift modeled here would produce insufficient aerosol optical depths, and any clouds that form will evaporate upon descent. Likewise, the difference in appearance between Neptune and Uranus may largely be due to the much lower relative humidity found at the tropopause in Uranus—evidently far less than saturation limited. Greater

lift is required to produce condensation, and this would require greater energy or greater tilt to isentropic surfaces due to greater temperature gradients across vortices. Recent activity in Uranus (dePater et al., 2014) might provide clues as to what changes result in high cloud variability. One possible explanation may involve the latent heat release associated with ortho-para hydrogen conversion as discussed in Smith and Gierasch (1995).

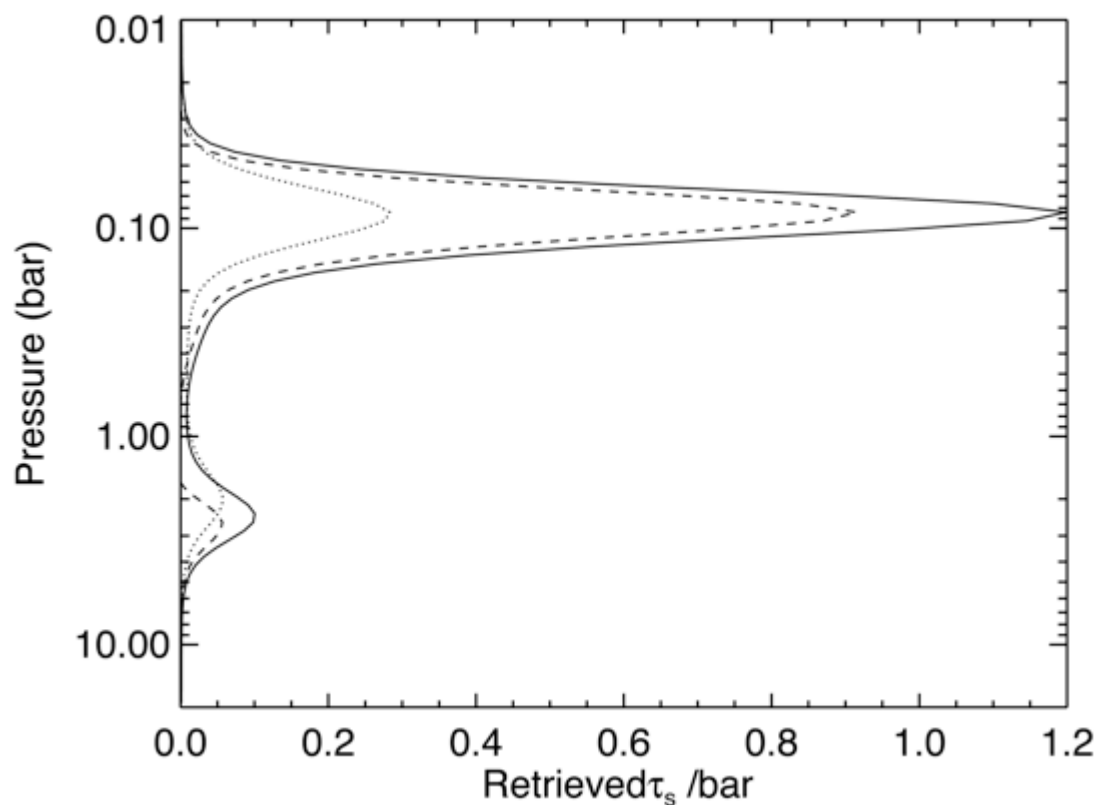


Figure 14. Mean aerosol profile at 40°S (solid), profile at 1°N (dotted), and the difference between the two (dashed) representing the effective scattering enhancement in regions of bright clouds.

Relatively higher clouds in Neptune’s northern hemisphere might indicate exaggerations of the same mechanisms at work as in the southern hemisphere. Since

both the upper and lower cloud layers are elevated in height, this would also imply that mechanisms causing this asymmetry extend over several scale heights. Temperature maps produced from Voyager IRIS data show a clear asymmetry in the heights of the coldest regions centered at $\sim 45^\circ$ N and S latitudes (Conrath et al., 1991; Fletcher et al., 2014). In the southern hemisphere, the coldest temperature contour is 52 K covers pressures from 200 mbar to 70 mbar; in the northern hemisphere, the same contour extends from ~ 170 to less than 40 mbar, with a minimum of < 50 K centered at roughly 80 mbar. Thus the latitudinal variation in retrieved scattering optical depths *and* cloud heights appear to be correlated with variation in the temperature field. It also has been argued that the variation in cloud heights is significant enough to suggest that completely different processes may produce them. Gibbard et al., (2003) argues that clouds above 60-mbar heights are closer expected levels of photolytic haze production as determined by Moses et al. (1992). Hence the highest clouds in the northern hemisphere may be hydrocarbon hazes as opposed to simple condensed methane. If this is true, this implies that more photochemical products evidently form in the winter hemisphere despite the seasonally diminished insolation relative to the southern hemisphere. This would suggest that dynamics may be cooling or concentrating species towards the winter pole. Unfortunately, given Neptune's lengthy orbital period, examining seasonal changes in the circulation and hazes require observations over many decades.

6. Concluding Summary

Spatially resolved, Near IR spectra of Neptune were analyzed to infer the atmospheric distribution of aerosols and methane. Retrievals are consistent with two layers of aerosol. The top layer shows significant temporal and spatial variability, existing at a height at or above the tropopause. The scattering optical depths of this layer were greatest at southern mid-latitudes, particularly in 2001 and 2002, though from 2003 to 2007, these latitudes diminished in reflectance. Similar variations have been noted by other researchers (e.g. Karkoschka, 2011), but the cause remains unknown. The retrieved heights and optical thicknesses are consistent with lift occurring in the lower stratosphere and thus consistent with models of slow upwelling and resultant anticyclonic vortex companion clouds as opposed to violent, penetrative convection.

The deeper cloud layer was relatively more uniform than the upper layer, but still displayed up to a factor of three variations in scattering optical depths. With a peak at ~ 2.3 bars, the greatest optical depths were also found at southern mid-latitudes in 2001 and 2002. Together, both layers suggest a circulation with upwelling at mid-latitudes with a vertical extent of several pressure scale heights, consistent with conclusions drawn from thermal, near-IR, and microwave data (Conrath et al., 1991; dePater et al., 2014).

The retrieved methane profiles show marginal temporal and spatial variability. All retrievals require a methane mole fraction in the lower stratosphere that exceeds the expected tropopause cold trap value. Higher methane mole fractions appear to be roughly correlated with latitudes of enhanced aerosols scattering optical depth and

theorized upwelling, though only marginally so given the retrieval uncertainties and apparent variability. The 60-mbar mole fractions are consistently less than other published values by a factor of 3 to 10. This may reflect differences in the observations as well as the modeling. Future analysis using different data and techniques may be necessary to better constrain the true value and explain the apparent discrepancy.

Finally, the temporal variation in high cloud cover on Neptune may be related to changes in the methane mole fraction. Such variations may ultimately result from changes in the intensity of upwelling. Periods of greater upwelling result in greater methane saturation and more cloud cover at mid-latitudes. The fact that Neptune has appeared more active than Uranus in past decades may be related to the difference in internal heat fluxes between the two planets; internal heating may drive circulation cells over greater vertical lengths on Neptune, pumping more methane higher into the atmosphere, ultimately leading to the prominent clouds and hazes that differentiate Neptune in appearance from Uranus.

Given the great distances and long seasons of the ice giants, increased understanding of the structure and dynamics of these worlds will only come through continued remote measurements of their observable features for decades to come. Leaps in our knowledge will ultimately require observations by future spacecraft missions, as we have seen for the other planets in our solar system.

REFERENCES

- Baines, Kevin H., and Jay T. Bergstralh. "The structure of the uranian atmosphere: Constraints from the geometric albedo spectrum and H₂ and CH₄ line profiles." *Icarus* 65.2 (1986): 406-441.
- Baines, Kevin H., and Heidi B. Hammel. "Clouds, hazes, and the stratospheric methane abundance in Neptune." *Icarus* 109.1 (1994): 20-39.
- Banfield, D., Gierasch, P. J., Squyres, S. W., Nicholson, P. D., Conrath, B. J., & Matthews, K. (1996). 2 μm spectrophotometry of jovian stratospheric aerosols—scattering opacities, vertical distributions, and wind speeds. *Icarus*, 121(2), 389-410.
- Banfield, D., Conrath, B. J., Gierasch, P. J., Nicholson, P. D., & Matthews, K. (1998). Near-IR spectrophotometry of jovian aerosols—Meridional and vertical distributions. *Icarus*, 134(1), 11-23.
- Borysow, A. (1996). Collision-induced absorption in the infrared: A database for modeling planetary and stellar atmospheres. *unpublished report updated annually*.
- Conrath, Barney J., Peter J. Gierasch, and Stephen S. Leroy. "Temperature and circulation in the stratosphere of the outer planets." *Icarus* 83.2 (1990): 255-281.
- Conrath, B. J., F. M. Flasar, and P. J. Gierasch. "Thermal structure and dynamics of Neptune's atmosphere from Voyager measurements." *Journal of Geophysical Research: Space Physics* (1978–2012) 96.S01 (1991): 18931-18939.
- Conrath, B. J. Gierasch, Ustinov, Thermal Structure and Para Hydrogen Fraction on the Outer Planets from Voyager IRIS Measurements (1998)
- de Kleer, K., Luszcz-Cook, S., de Pater, I., Ádámkovics, M., & Hammel, H. B. (2015). Clouds and aerosols on Uranus: Radiative transfer modeling of spatially-resolved near-infrared Keck spectra. *Icarus*, 256, 120-137.
- de Pater, Imke, Paul N. Romani, and Sushil K. Atreya. "Possible microwave absorption by H₂S gas in Uranus' and Neptune's atmospheres." *Icarus* 91.2 (1991): 220-233.
- de Pater, Imke, et al. "Neptune's global circulation deduced from multi-wavelength observations." *Icarus* 237 (2014): 211-238.
- de Pater, Imke, et al. "Record-breaking storm activity on Uranus in 2014." *Icarus* 252 (2015): 121-128.

Fletcher, Leigh N., et al. "Neptune's atmospheric composition from AKARI infrared spectroscopy." *Astronomy & Astrophysics* 514 (2010): A17.

Fletcher, Leigh N., et al. "Saturn's tropospheric composition and clouds from Cassini/VIMS 4.6–5.1 μm nightside spectroscopy." *Icarus* 214.2 (2011): 510-533.

Fletcher, Leigh N., et al. "Neptune at summer solstice: Zonal mean temperatures from ground-based observations, 2003–2007." *Icarus* 231 (2014): 146-167.

Fry, P. M., Sromovsky, L. A., De Pater, I., Hammel, H. B., & Rages, K. A. (2012). Detection and tracking of subtle cloud features on Uranus. *The Astronomical Journal*, 143(6), 150.

Gibbard, S. G., et al. "The altitude of Neptune cloud features from high-spatial-resolution near-infrared spectra." *Icarus* 166.2 (2003): 359-374.

Hammel, H. B., and G. W. Lockwood. "Atmospheric structure of Neptune in 1994, 1995, and 1996: HST imaging at multiple wavelengths." *Icarus* 129.2 (1997): 466-481.

Hansen, James E., and Larry D. Travis. "Light scattering in planetary atmospheres." *Space Science Reviews* 16.4 (1974): 527-610.

Hayward, T. L., Brandl, B., Pirger, B., Blacken, C., Gull, G. E., Schoenwald, J., & Houck, J. R. (2001). PHARO: A Near-Infrared Camera for the Palomar Adaptive Optics System. *Publications of the Astronomical Society of the Pacific*, 113(779), 105-118.

Herzberg, G. "Spectroscopic evidence of molecular hydrogen in the atmospheres of Uranus and Neptune." *The Astrophysical Journal* 115 (1952): 337-340.

Hunten, D. M. (1974). Energetics of thermospheric eddy transport. *Journal of Geophysical Research*, 79(16), 2533-2534.

Hofstadter, Mark D., and Bryan J. Butler. "Seasonal change in the deep atmosphere of Uranus." *Icarus* 165.1 (2003): 168-180.

Irwin, P. G. J., N. A. Teanby, and G. R. Davis. "Vertical cloud structure of Uranus from UKIRT/UIST observations and changes seen during Uranus' Northern Spring Equinox from 2006 to 2008." *Icarus* 203.1 (2009): 287-302.

Irwin, P. G. J., N. A. Teanby, and G. R. Davis. "Revised vertical cloud structure of Uranus from UKIRT/UIST observations and changes seen during Uranus' Northern Spring Equinox from 2006 to 2008: Application of new methane absorption data and comparison with Neptune." *Icarus* 208.2 (2010): 913-926.

Irwin, P.J.G, N.A. Teanby, G.R. Davis, L.N. Fletcher, G.S. Orton, S.B. Calcutt, D.S. Tice, J. Hurley, Further seasonal changes in Uranus' cloud structure observed by Gemini-North and Ukirt (2012a)

Irwin, P.J.G., C. de Bergh, R. Courtin... The application of new methane line absorption data to Gemini-N/NIFS and KPNO/FTS observations of Uranus' near-infrared spectrum (2012b)

Irwin, P.J.G, N.A. Teanby, G.R. Davis, L.N. Fletcher, G.S. Orton, S.B. Calcutt, D.S. Tice, J. Hurley, Further seasonal changes in Uranus' cloud structure observed by Gemini-North and Ukirt (2012a)

Irwin, P. G. J., et al. "Reanalysis of Uranus' cloud scattering properties from IRTF/SpeX observations using a self-consistent scattering cloud retrieval scheme." *Icarus* 250 (2015): 462-476.

Karkoschka, Erich. "Clouds of high contrast on Uranus." *Science* 280.5363 (1998): 570-572.

Karkoschka, Erich. "Uranus' apparent seasonal variability in 25 HST filters." *Icarus* 151.1 (2001): 84-92.

Karkoschka, Erich, and Martin Tomasko. "Saturn's vertical and latitudinal cloud structure 1991–2004 from HST imaging in 30 filters." *Icarus* 179.1 (2005): 195-221.

Karkoschka, Erich, and Martin Tomasko. "The haze and methane distributions on Uranus from HST-STIS spectroscopy." *Icarus* 202.1 (2009): 287-309.

Karkoschka, Erich. "Neptune's cloud and haze variations 1994–2008 from 500 HST-WFPC2 images." *Icarus* 215.2 (2011): 759-773.

Karkoschka, Erich, and Martin G. Tomasko. "The haze and methane distributions on Neptune from HST–STIS spectroscopy." *Icarus* 211.1 (2011): 780-797.

Karkoschka, Erich. "Uranus' southern circulation revealed by Voyager 2: Unique characteristics." *Icarus* 250 (2015): 294-307.

Lellouch, E., et al. "First results of Herschel-PACS observations of Neptune." *Astronomy & astrophysics* 518 (2010): L152.

Lindal, G. F., Lyons, J. R., Sweetnam, D. N., Eshleman, V. R., Hinson, D. P., & Tyler, G. L. (1987). The atmosphere of Uranus: Results of radio occultation measurements with Voyager 2. *Journal of Geophysical Research: Space Physics* (1978–2012), 92(A13), 14987-15001.

- Lindal, G. F., et al. "The atmosphere of Neptune: Results of radio occultation measurements with the Voyager 2 spacecraft." *Geophysical Research Letters* 17.10 (1990): 1733-1736.
- Lockwood, G. W., and Mikołaj Jerzykiewicz. "Photometric variability of Uranus and Neptune, 1950–2004." *Icarus* 180.2 (2006): 442-452.
- Lunine, Jonathan I., and Donald M. Hunten. "Abundance of condensable species at planetary cold traps: The role of moist convection." *Planetary and space science* 37.2 (1989): 151-166.
- Morrison, David, and Dale P. Cruikshank. "Temperatures of Uranus and Neptune at 24 microns." *The Astrophysical Journal* 179 (1973): 329-332.
- Moses, Julianne I. "Meteoroid ablation in Neptune's atmosphere." *Icarus* 99.2 (1992): 368-383.
- Irwin, P.J.G. , D. S. Tice, L.N. Fletcher, J.K. Barstow, N.A. Teanby, G.S. Orton, G.R. Davis. Reanalysis of Uranus' cloud scattering properties from IRTF/SpEx observations using a self-consistent scattering cloud retrieval scheme (2012)
- Orton, Glenn S., et al. "Evidence for methane escape and strong seasonal and dynamical perturbations of Neptune's atmospheric temperatures." *Astronomy & Astrophysics* 473.1 (2007): L5-L8.
- Orton, Glenn S., et al. "Mid-infrared spectroscopy of Uranus from the Spitzer infrared spectrometer: 2. Determination of the mean composition of the upper troposphere and stratosphere." *Icarus* 243 (2014): 471-493.
- Pérez-Hoyos, S., et al. "Saturn's cloud structure and temporal evolution from ten years of Hubble Space Telescope images (1994–2003)." *Icarus* 176.1 (2005): 155-174.
- Rages, K. A., et al. "Variability on Uranus and Neptune during HST Cycle 9." *Bulletin of the American Astronomical Society*. Vol. 33. 2001.
- Roe, Henry G., et al. "The altitude of an infrared-bright cloud feature on Neptune from near-infrared spectroscopy." *The Astronomical Journal* 122.2 (2001): 1023.
- Smith, Bradford A., et al. "Voyager 2 in the Uranian system: Imaging science results." *Science* 233.4759 (1986): 43-64.
- Smith, B. A., Soderblom, L. A., Banfield, D., Barnet, C., & Basilevsky, A. T. (1989). Voyager 2 at Neptune: Imaging science results. *Science*, 246(4936), 1422.
- Smith, Michael D., and Peter J. Gierasch. "Convection in the outer planet atmospheres including ortho-para hydrogen conversion." *Icarus* 116.1 (1995): 159-179.

Sromovsky, Lawrence A., Sanjay S. Limaye, and Patrick M. Fry. "Clouds and circulation on Neptune: Implications of 1991 HST observations." *Icarus* 118.1 (1995): 25-38.

Sromovsky, L. A., et al. "Ground-based observations of cloud features on Uranus." *Icarus* 146.1 (2000): 307-311.

Sromovsky, L. A., P. M. Fry, and K. H. Baines. "The unusual dynamics of northern dark spots on Neptune." *Icarus* 156.1 (2002): 16-36.

Sromovsky, L. A., and P. M. Fry. "Keck 2 AO Observations of Uranus in 2004." *Bulletin of the American Astronomical Society*. Vol. 36. 2004.

Sromovsky, L. A., and P. M. Fry. "Dynamics of cloud features on Uranus." *Icarus* 179.2 (2005): 459-484.

Sromovsky, L. A., and P. M. Fry. "Spatially resolved cloud structure on Uranus: Implications of near-IR adaptive optics imaging." *Icarus* 192.2 (2007): 527-557.

Sromovsky, L. A., et al. "Dynamics, evolution, and structure of Uranus' brightest cloud feature." *Icarus* 192.2 (2007): 558-575.

Sromovsky, L. A., et al. "Uranus at equinox: Cloud morphology and dynamics." *Icarus* 203.1 (2009): 265-286.

Sromovsky, L. A., P. M. Fry, and Joo Hyeon Kim. "Methane on Uranus: The case for a compact CH₄ cloud layer at low latitudes and a severe CH₄ depletion at high-latitudes based on re-analysis of Voyager occultation measurements and STIS spectroscopy." *Icarus* 215.1 (2011): 292-312.

Sromovsky, L. A., et al. "Comparison of line-by-line and band models of near-IR methane absorption applied to outer planet atmospheres." *Icarus* 218.1 (2012): 1-23.

Sromovsky, L. A., et al. "Methane depletion in both polar regions of Uranus inferred from HST/STIS and Keck/NIRC2 observations." *Icarus* 238 (2014): 137-155.

Stam, Daphne M., et al. "Near-IR spectrophotometry of saturnian aerosols—Meridional and vertical distribution." *Icarus* 152.2 (2001): 407-422.

Stoker, Carol R., and Owen B. Toon. "Moist convection on Neptune." *Geophysical research letters* 16.8 (1989): 929-932.

Stratman, Paul William, et al. "EPIC simulations of bright companions to Neptune's Great Dark Spots." *Icarus* 151.2 (2001): 275-285.

Tice, Dane S., et al. "Uranus' cloud particle properties and latitudinal methane variation from IRTF SpeX observations." *Icarus* 223.2 (2013): 684-698.

van de Hulst, H. C. *Light scattering by small particles*. Courier Corporation, 1957.

Weast, Robert C. "Handbook of Chemistry and Physics 67th, ed." Chemical Rubber Co., Cleveland, OH (1987).